ASTROMETRIC DETECTION OF INTERMEDIATE-MASS BLACK HOLES IN THE GALACTIC CENTER

A Thesis

Presented to the Department of Astronomy

of Harvard College

in Partial Fulfillment of the Requirements for the Degree of

Bachelor of Arts

by

Eden Girma

May 2018

ASTROMETRIC DETECTION OF INTERMEDIATE-MASS BLACK HOLES IN THE GALACTIC CENTER

Eden Girma, B.A.

Harvard College 2018

So far, black holes have been conclusively detected within only two mass ($M_{\rm BH}$) ranges: stellar-mass (where $3\ M_\odot \leq M_{\rm BH} \leq 100\ M_\odot$) and supermassive ($10^6\ M_\odot \leq M_{\rm BH} \lesssim 10^{10}\ M_\odot$). Intermediate-mass black holes (IMBHs, $100\ M_\odot \leq M_{\rm BH} \leq 10^6\ M_\odot$) represent a missing component that could provide essential insights into black hole formation, evolution, and dynamics. Dynamical signatures of IMBHs have mainly been studied in globular clusters, but dynamical friction could bring such clusters over time to the galactic center. The presence of these higher mass objects may be identified by their effect on the motion of the central black hole Sgr A* or stars around it. In this thesis I investigate, given a possible density profile for a black hole population in the inner parsec of the Milky Way galaxy, whether the effect of these black holes on the phase space of Sgr A* and the orbital parameters of the star S2 is detectable with recent innovations in astrometry while necessarily fitting within current observational constraints. I find that the IMBH profile provided by Mastrobuono-Battisti et al. (2014), which distributes ~ 10 $10^4\ M_\odot$ IMBHs within one parsec, induces the largest angular shift of $\sim 65\ \mu$as yr^{-1} on the position of Sgr A*, corresponding to a perpendicular velocity component magnitude of 1.6 km s^{-1}. Additionally this profile is the only one from the profiles examined to induce changes in the orbit of S2 that surpass those induced by general relativity, generating a mean angular shift in periapse and apoapse of 62 μas and 970 μas respectively.

BIOGRAPHICAL SKETCH

Eden Girma is the child of Ethiopian immigrants, raised in Madison, WI. At Harvard College, Eden joint concentrates in Astrophysics and Math with a secondary in Music, and additionally pursues a Masters in Music at the New England Conservatory. Designated as a Mellon Mays undergraduate research fellow in 2016, Eden has worked under the direction of Professor Avi Loeb, Professor John Johnson, and Dr. James Guillochon.

ACKNOWLEDGEMENTS

To Avi Loeb, for his incredibly thoughtful guidance in all our work together during my undergraduate career,

To the Mellon-Mays Foundation, for their financial support of the research contributing to this work,

To John Johnson, Jorge Moreno, and the entire Banneker-Aztlán community for their support and inspiration for me a young astronomer of color,

To Nia Imara, for her kind mentorship and continual demonstration that astronomy, art, and social activism need not be mutually exclusive,

To Lauren Nicholson, Shantell Williams, Jessie Laurore, and Janae Bell, for all the love and care they have extended to me these past four years,

To the Center for High Energy Metaphysics, an intellectual hub I could not survive Harvard without,

And lastly, to my family and particularly my parents, whose continual sacrifices have made my life possible. **በእናንተ: ምክንያት፡ እንደ፡ ንስር፡ በክንፍ፡ እወጣለሁ።**

TABLE OF CONTENTS

LIST OF TABLES

LIST OF FIGURES

CHAPTER 1

INTRODUCTION

1.1 Brief Review of Black Holes

Black holes have been objects of inquiry ever since their mathematical discovery in the solutions of Einstein's field equations of general relativity. Their simplicity, being described solely by gravitational mass, angular momentum, and electric charge (Israel, 1967) make them particularly significant in fundamental physics and astrophysics. While black hole theory has been developed mathematically, an astrophysical understanding of these objects is so far incomplete. Black holes have been conclusively detected within two mass ($M_{\rm BH}$) ranges – stellar-mass (where $3\ M_\odot \leq M_{\rm BH} \leq 100\ M_\odot$) and supermassive ($10^6\ M_\odot \leq M_{\rm BH} \lesssim 10^{10}\ M_\odot$) – but are theoretically capable of existing at any mass.

Stellar-mass black holes are the end result of a gravitationally collapsing massive star. Through careful observation of close binaries, one can detect stellar-mass black holes by their X-ray radiation, given that the derived primary mass exceeds the (extremely conservative) neutron star upper mass limit of $3\ M_\odot$. The first of such evidence was found between the 1970s and 1980s (e.g. Cygnus X-1, see Webster & Murdin, 1972), and more recently black holes of order $10\ M_\odot$ have been detected through gravitational waves produced from their mergers. (e.g. GW150914, see Abbott et al., 2016).

Supermassive black holes (SMBHs) have been identified in the centers of nearly all massive galaxies, and are distinguished by their extremely high mass (on the order of 10^6 or higher) and low density (see reviews by Kormendy & Ho, 2013;

McConnell & Ma, 2013; Graham, 2016). At the center of the galaxy, a SMBH will continue to grow through accretion of matter and black hole mergers. A tight correlation between SMBH mass and the velocity dispersion of surrounding stars suggests a "principle of self regulation", which limits the final black hole mass due to the gravitational potential-well depth of its host spheroid (see Di Matteo et al., 2005, and references therein) to $\sim 10^{10}\ M_{\odot}$ (Natarajan & Treister, 2009). The majority of SMBHs are viewed as dormant, while active galactic nuclei (AGN), observed as bright sources at the center of a galaxy, are often associated with SMBHs accreting gas from the host galaxy's core. Quasars are the most powerful and point-like of AGN, being observed out to very high redshifts ($z \sim 7.5$, ~ 0.7 Gyr after the Big Bang) (Loeb & Furlanetto, 2013; Bañados et al., 2018).

The initial formation mechanism of SMBHs still remains a mystery, though an obvious model involves $10 - 100\ M_{\odot}$ "seeds" that form from the deaths of massive stars and grow via accretion. However, SMBHs pose a particular physical hurdle of needing enough matter within a very constrained volume, necessitating that the matter has little angular momentum. Hence slower accretion processes would limit the growth rate of an SMBH. Given that SMBHs on order of $10^5\ M_{\odot}$ had already formed by redshift $z \approx 7.5$ (which is inferred through observation of quasars, see Loeb & Furlanetto, 2013; Bañados et al., 2018), supermassive black holes more likely emerged in the early Universe within the very first massive galaxies and involved rapid gas accretion observable in AGN. Hydrodynamical simulations of the period before re-ionization have indicated that low-spin and metal free galaxies with viral temperatures of $\sim 10^4$ K and suppressed H_2 formation will form a single central black hole (Bromm & Loeb, 2003). Additional formation models involve dynamical interactions such as black hole binaries or relativistic instabilities (see Begelman et al., 1984).

The currently observed mass distribution of black holes possesses an absence of *intermediate-mass black holes* (IMBHs), black holes of masses from $10^2 - 10^5\ M_\odot$. They are too massive to be formed from the collapse of present-day stars, and their supposed environments lack the high density and velocities that could potentially fuel SMBH growth. Circumstantial evidence has identified potential IMBH candidates, though there has yet to be any certain dynamical mass measurements. Despite the relatively weak observational evidence, IMBHs continue to represent a critical missing link between stellar and supermassive black holes, and a definitive discovery could provide essential insights into black hole formation, evolution, and dynamics.

Thus far, 4 distinct hypotheses for IMBH formation mechanisms have been proposed in the literature:

1. *The direct collapse of very massive Population III stars.* Population III stars necessarily formed out of unmagnetized and metal-free gas, and from recent numerical simulations are further suggested to possess a characteristic mass $m \geq 200\ M_\odot$ (Bromm et al., 1999; Abel et al., 2000; Figer et al., 1996). Such a star could then collapse to a massive black hole of at least half the initial stellar mass (Madau & Rees, 2001).

2. *Runaway mergers within dense stellar clusters.* A number of star clusters has been discovered within 100 parsecs (pc) of the Galactic Center, opening new research into the relation between these clusters, the inner 100 pc of the Galactic Center, and the development of the Milky Way's central SMBH. Semi-analytical N-body simulations of a variety of such star clusters demonstrate that, as star clusters sinks inward towards the Galactic Center, a collision runaway star can form and grow via repeated stellar collisions. This

runaway system then collapses to an IMBH of characteristic mass 1000 $M_\odot$ (Zwart et al., 2006).

3. *Gas accretion from primordial globular clusters on to stellar-mass black holes.* This hypothesis was initially developed by Leigh et al. (2013) to explain the variety of stellar populations within a single globular cluster, arguing that accretion of the interstellar medium onto stellar-mass black holes can be an adequate mechanism for removing gas produced from initial star formation. The process would lead to a large increase of the black holes' mass, hastening their mass segregation and ultimately the formation of IMBH seeds.

4. *Stochastic formation via mergers and mass transfers.* Based on results of the Monte Carlo Cluster Simulator (MOOCA) simulations of dense stellar systems developed by Giersz et al. (2016), IMBHs are formed solely through mass transfers in black hole binaries and black hole mergers. While these processes require no particular special conditions to begin, they are inherently random, with the larger cluster concentrations corresponding to higher probability of IMBH formation on smaller time scales.

Currently, two types of data suggest the existence of IMBHs: Ultraluminous X-ray sources and observations of globular clusters. Ultraluminous X-ray Sources (ULXs) refer to compact, accreting X-ray sources with luminosities exceeding those of any known stellar process ($> 10^{39}$ erg s^{-1}). Generally, active black holes are often candidates of ULXs as they emit X-rays via accretion. Accreting matter forms a thin disk around a black hole with inner boundary of $r_{\rm in} \sim 3\ R_{\rm sch}$. Here, $R_{\rm sch} = 2GM_{\rm BH}/c^2$ is the Schwarzchild radius, making $r_{\rm in}$ directly proportional to the black hole mass:

$$r_{\rm in} \sim 3\left(2\frac{GM_{\rm BH}}{c^2}\right) \approx 9\left(\frac{M_{\rm BH}}{M_\odot}\right)\ \text{km} \tag{1.1}$$

Assuming that the X-rays are emitted isotropically, a black hole's luminosity is constrained by the balance of outward radiative forces and inward gravitational forces. The upper limit extrapolated from this constraint is known as the Eddington Luminosity:

$$L_{\mathrm{Edd}} = \frac{4\pi G M_{\mathrm{BH}} m_{\mathrm{p}} c}{\sigma_T} = 1.26 \times 10^{38} \left(\frac{M_{\mathrm{BH}}}{M_\odot} \right) \mathrm{erg\ s^{-1}} \tag{1.2}$$

where $\sigma_T = 6.65 \times 10^{-25}$ cm^2 is the Thomson scattering cross section for an electron and we suppose the accreted stellar material is pure ionized hydrogen. Note that anisotropic accretion or radiation can produce luminosities that arbitrarily exceed the Eddington luminosity.

Efforts to understand the true nature of observed ULXs have depended on estimating their compact object masses. Such progress has been made through analyzing quasi-periodic oscillations (QPOs) of ULXs, which are characterized as frequency peaks in the power spectrum of ULX light curves. Pairs of high-frequency QPOs (100-450 HZ) occurring in a 3:2 ratio have been associated with stellar-mass black holes, and appear to scale inversely with the black hole mass (Remillard & McClintock, 2006; Belloni et al., 2012). One can posit the existence of analogous 3:2 high-frequency QPOs from IMBHs under the black hole unification paradigm, which attempts to understand how AGN evolve over cosmological timescales by studying similar properties within the more rapid evolution of black hole X-ray binary systems (Vaughan & Uttley, 2005). Mass estimates for the IMBH candidates M82 X-1 and NGC 1313 X-1 have been extrapolated from such QPO measurements (Pasham et al., 2014, 2015). However, it is important to recognize that such these are only rough estimations; there has been no direct measurement of compact source masses.

Kinematic data from observed galactic centers has additionally offered esti-

mates of black hole masses in distant galaxies, and particularly for IMBHs in low-mass galaxies, AGN, and globular clusters. There is an tight empirical correlation, known as the $M-\sigma$ relation, between central black hole mass and velocity dispersion of its host spheroid of stars (Ferrarese & Merritt, 2000; Gebhardt et al., 2000). Using a complete sample of black hole masses in nearby galaxies, McConnell et al. (2011) gives the relation as:

$$\frac{M_{\rm BH}}{10^8\ M_\odot} \approx 1.9 \left(\frac{\sigma}{200{\rm km\ s^{-1}}}\right)^{5.1} \tag{1.3}$$

In accordance with this relation, massive black holes in the center of globulars would theoretically affect the distribution function of stars, producing cusps in velocity and density. Therefore, observation of these cusps in globular clusters could indirectly confirm the existence of IMBHs. Graham et al. (2001) presented a strong correlation between bulge concentration and mass of a central supermassive black hole, finding that the central radial concentration of light correlates strongly with black hole mass. This correlation was re-investigated and re-described by Graham & Driver (2007) as a log-quadratic relation between black hole mass and Sérsic index n (a measure of concentration), with a break in slope of the relation between low- and high- mass ends. While there is inarguably a $M_{\rm bh}-n$ relation due to the existence of a mass-luminosity relation (e.g. Young & Currie, 1994; Jerjen et al., 2000) and luminosity-n relation, several studies have failed to recover the relation obtained by Graham et al. (2001) when reviewing galaxies with directly measured black hole masses. This is due to significantly varying measurements of the Sérsic index for a particular galaxy between authors (e.g. Laurikainen et al., 2010; Sani et al., 2011; Vika et al., 2012) (see Savorgnan et al., 2013, for a census of Sérsic index measurements for local galaxies with directly measured SMBH mass).

Gebhardt et al. (2002) used Hubble observations to report stellar distributions in the globular cluster M31-G1 that favor a $\sim 2 \times 10^4\ M_\odot$ black hole, significant at the 1.5σ level. However, their significance is dependent on extensive N-body modeling of such clusters that has not been thoroughly pursued (Coleman Miller & Colbert, 2004). A more recent and promising method for detecting IMBHs in globular clusters uses the monitoring of pulsars to identify or constrain an IMBH's dynamical signature. Kızıltan et al. (2017) combine measurements of pulsars detected in the globular cluster 47 Tucanae (NGC 104) with different dynamical N-body simulations to quantify what distribution is most likely associated with the observed range of pulsar accelerations, and their best fit model suggests central black hole with a mass of $2,300^{+1,500}_{-850}\ M_\odot$ while independently and consistently measuring a total cluster mass of $0.76 \times 10^6\ M_\odot$. Similarly, Perera et al. (2017) utilized timing observations of a millisecond pulsar in the globular cluster NGC 6624 and the cluster's mass properties to argue the existence of a IMBH with mass $> 7,500\ M_\odot$.

1.2 Cluster Systems

Clusters, being discontinuous dynamical systems, experience complex effects induced by the discrete nature of their components and the interactions occurring between them. Gravitationally bound clusters are characterized by a relaxation time τ_r, during which a test object changes its velocity by an order itself due to random perturbations induced by surrounding gravitational fields. Chandrasekhar (1941) first estimated this timescale as

$$\tau_r \sim \frac{\sigma^3}{8\pi G^2 \mu^2 n \ln \Lambda} \tag{1.4}$$

where μ is stellar mass, σ is the velocity dispersion, n is the number of stars per unit volume, and Λ is the ratio of the maximal and minimal impact parameters, $b_{\max}$ and $b_{\min}$. For a virialized and self-gravitating system, the typical $b_{\min}$ (which leads to a deflection angle of $\pi/2$) is $G\langle m_* \rangle/\sigma^2$, and $b_{\max}$ is on the order of the half-mass radius R_h (Freitag et al., 2006). Regions where the gravitational field is dominated by a central object with mass $M_\bullet$ and characterized by an average stellar mass $\langle m_* \rangle$ possess a Λ of approximately $M_\bullet/\langle m_* \rangle$.

In idealizing relaxation as the sum of a large number of independent two-body encounters, one can define an additional expression for relaxation time in terms of velocity dispersion σ, number density n, and average stellar mass $\langle m_* \rangle$ (Freitag et al., 2006):

$$\tau_{\rm r} = \frac{\sqrt{2}\pi}{64} \frac{\sigma^3}{G^2 \langle m_* \rangle^2 n \ln \Lambda} \tag{1.5}$$

$$= 3.67 \times 10^8 \text{ yr } \left(\frac{\sigma}{100 \text{ km s}^{-1}} \right)^3 \left(\frac{n}{10^6 \text{ pc}^{-3}} \right)^{-1} \left(\frac{\langle m_* \rangle}{M_\odot} \right)^{-1} \left(\frac{\ln \Lambda}{10} \right)^{-1} \tag{1.6}$$

This equation is constructed such that a particle of mass $\langle m_* \rangle$, traveling for a time dt at a velocity $v = \sqrt{2}\sigma$ through a field of particles of the same mass, would be deflected by an angle $d\theta$, with $\langle d\theta \rangle = (\pi/2)^2 dt/\tau_{\rm rlx}$. In the scenario when $\ln \Lambda$ is essentially constant, more massive objects will experience a steady deceleration due to dynamical friction. Assuming a spherical density distribution, the total acceleration of a larger mass object M is G/v_M^2 times the total mass of lower-mass objects m with velocities $v_m < v_M$. The acceleration of M can be solved for, given that the smaller mass objects are isotropically distributed in phase space:

$$\frac{d\vec{v}_M}{dt} = -16\pi^2 \ln \Lambda G^2 m(M+m) \frac{\int_0^{v_M} f(r,v) v^2 dv}{v_M^3} \vec{v}_m \tag{1.7}$$

Equation 1.7 is known as the *Chandrasekhar dynamical friction formula*, derived for a mass that travels through an infinite and homogeneous background (Chandrasekhar, 1943). Due to this frictional force, larger mass objects in an otherwise

homogeneous stellar cluster will over time migrate to the center of the system. Analogously, a cluster is equally subject to dynamical friction as it orbits the host galaxy center with a velocity v_c, and eventually spirals inwards from an initial radius r_i and mass M after a time (Binney & Tremaine, 2011, eq. 7-25)

$$\begin{aligned} t_{fric} &= \frac{1.17}{\ln \Lambda} \frac{r_i^2 v_c}{GM} \\ &= 2.64 \times 10^{10} \text{ yr } \left(\frac{\ln \Lambda}{10}\right)^{-1} \left(\frac{r_i}{2 \text{ kpc}}\right)^2 \left(\frac{v_c}{250 \text{ km s}^{-1}}\right) \left(\frac{M}{10^6 \ M_\odot}\right)^{-1} \end{aligned} \tag{1.8}$$

Bahcall & Wolf (1976) first approximated the effects of relaxation on the final density profile for a simplified case of a spherical cluster with a central massive black hole (MBH). They applied a Fokker-Planck treatment to describe the evolution of a particle's velocity probability density function when experiencing drag and random forces, ultimately finding a $r^{-7/4}$ power law for the equilibrium stellar density. The treatment discounted stars on elongated orbits, and assumed stars are destroyed only through reaching a high binding energy (e.g. significant star-star collisions or tidal disruptions). Additionally, their idealization corresponded to an isotropic phase space distribution

$$f(\vec{r}, \vec{v}, t) d\vec{r} d\vec{v} = \text{mass in } d\vec{r} d\vec{v} \tag{1.9}$$

from which one calculates the number of particles per unit volume in coordinate space, per unit volume in velocity space. In an N-body system, such a phase space distribution implies there is a zero net diffusive flux of particles in energy space, implying that the phase space distribution can be written as only a function of energy per unit mass. In general, given a spherically symmetric density distribution, we can recover a phase space distribution function that depends only on energy and generates a given density profile ρ with potential Φ (Binney & Tremaine, 2011, Eq. 4-140b):

$$f(\mathcal{E}) = \frac{1}{\sqrt{8}\pi^2} \frac{d}{d\mathcal{E}} \int_0^{\mathcal{E}} \frac{d^2\rho}{d\Phi^2} \frac{d\Phi}{\sqrt{\mathcal{E} - \Phi}} \tag{1.10}$$

Conversely, we can find the density profile of a system given the phase space distribution of that system and potential Φ (Binney & Tremaine, 2011, eq. 4-138):

$$\rho(r) = 4\pi \int_0^{\Phi} f(\mathcal{E})\sqrt{2(\Phi - \mathcal{E})}d\mathcal{E} \tag{1.11}$$

Similar to Bahcall & Wolf, Shapiro & Lightman (1976) analytically derive a $\rho \propto r^{-7/4}$ cusp that surrounds a central black hole. Letting t_S(r) and $t_U(r)$ denote the net star and net energy diffusion timescales at a radius r respectively, we have from dynamic equilibrium that for a general N-body system, $t_U(r) \propto t_S(r)E(r)$, where $E(r)$ is the mean energy per unit mass at r. In this particular scenario $E(r) \sim -GM/r$, giving

$$t_U(r) \propto t_S(r)r^{-1} \tag{1.12}$$

Supposing a steady state system, stars are disrupted and consumed upon reaching the tidal radius of the black hole,

$$r_t \simeq R_\star(M_{\rm BH}/M_\star)^{1/3} \tag{1.13}$$

where $M_\star$ and $R_\star$ are the stellar mass and radius respectively. This consumption is countered by a net inward flux of stars migrating from beyond the central region, which replaces disrupted stars and maintains the stellar distribution. The net energy flux U can be solved for given a stellar density $\rho(r)$:

$$U \sim \frac{\rho(r)r^3E(r)}{t_U(r)} = \frac{-\rho(r)r^2GM}{t_U(r)} = \text{constant} \tag{1.14}$$

Due to the lack of outgoing stars at r_t, the net diffusion time from $2r_t$ to r_t must equal the timescale for their energy to decrease by a factor of 2. This implies $t_U(r_t) \sim t_S(r_t)$, which when taking Equation 1.12 gives us

$$t_U(r) \sim \left(\frac{r_t}{r}\right) t_S(r)r \tag{1.15}$$

t_U can be equated to the relaxation timescale $\tau_r \propto \sigma^{3/2}/(G^2 m^2 \rho)$ (Equation 1.4) for $r > r_t$. As $\sigma^2 \sim GM/r$ for bound stars near a black hole, we can combine the above equation with Equation 1.14 to yield $\rho(r) \propto r^{-7/4}$. The findings of Bahcall and Wolf have been further supported by more detailed Fokker-Planck treatments that accounted for various bounding conditions such as loss-cone effects (Bahcall & Wolf, 1977; Lightman & Shapiro, 1977; Cohn & Kulsrud, 1978). Monte-Carlo codes have also demonstrated a $r^{-7/4}$ cusp forming from diffusive, local relaxation, taking into consideration disruptive and non-disruptive collisions (Shapiro, 1985; Freitag & Benz, 2002).

In this work we are concerned with such systems, present in the the centers of galaxies and in particular AGNs. These systems are characterized by centralized powerful energy sources, which possess luminosities on the order of 10^{46} erg s^{-1} (over a trillion times the luminosity of the sun) while covering regions spanning less than a light year ($\sim 10^{18}$ cm). Their compactness and energy radiation cannot reasonably be explained by any stellar-related processes, and suggest the presence of a relativistic potential only associated with black holes. The black hole model for galactic nuclei was first theorized by Lynden-Bell & Rees (1971), though beginning with Sandage (1965) astronomers have attempted to prove the existence of massive central black holes through photometric and spectrographic measurements. Decades would pass before observations were reliable enough to rule out alternative theories, and the most conclusive evidence of SMBHs first came from the following observational works: Tanaka et al. (1995), who detected a highly asymmetric and predominately red-shifted X-ray emission line that could have only been broadened relativistically; and Miyoshi et al. (1995), who used very long baseline interferometry (VLBI) to detect an extremely dense central object in the galaxy NGC 4258 (that required a mass of 3.6×10^7 $M_\odot$ within only 0.13

parsec!)

Forces in the center of our own galaxy are dominated by the potential of a $\sim 4 \times 10^6\ M_\odot$ compact radio source (Gillessen et al., 2009; Ghez et al., 2008) Sagittarius A* (Sgr A*), first discovered by Balick & Brown (1974). Through high-resolution infra-red monitoring of the orbits of stars in the innermost arc-second (referred to as S-stars), Schödel et al. (2002); Eisenhauer et al. (2005); Ghez et al. (2005); and Gillessen et al. (2009) were able to confirm previous hypotheses developed from proper motion and radial velocity surveys (see Lacy et al., 1979, 1980; Eckart & Genzel, 1996, 1997; Genzel et al., 1996, 1997; Ghez et al., 1998) that Sgr A* is in fact a supermassive black hole. Its radius of influence, confirmed in observations by Merritt & Ferrarese (2001), has been analytically solved for by Peebles (1972, Eq. 19):

$$\begin{aligned} r_{\rm infl} &= \frac{GM_{\rm bh}}{\sigma^2} \\ &= 1.19\ {\rm pc} \left(\frac{M_{\rm bh}}{4 \times 10^6\ M_\odot} \right) \left(\frac{\sigma}{120\ {\rm km\ s^{-1}}} \right)^{-2} \end{aligned} \tag{1.16}$$

where σ is the characteristic velocity dispersion of the cluster system.

1.3 Stellar- and Intermediate-mass Black Holes in Clusters

To extend knowledge of stellar and cluster dynamics, astronomers have naturally sought an understanding of clusters containing stellar-mass black holes and potential intermediate-mass black holes. Stars of mass $\gtrsim 30\ M_\odot$ can collapse to become stellar-mass black holes with a median mass of 7 $M_\odot$ (Bailyn et al., 1998). As a consequence of dynamical friction, these comparatively higher mass objects will sink to the Galactic Center on time scales within a Hubble time (Morris, 1993).

The resulting mass segregation then produces a collection of black holes concentrated within the inner parsec. Miralda-Escudé & Gould (2000) calculated that, assuming a characteristic mass of 7 $M_\odot$ for stellar black holes and velocity dispersion data fit by Genzel et al. (2000), a cluster of approximately 20,000 black holes will form around Sgr A*. This relaxes to a density profile reflecting the Bahcall-Wolf cusp,

$$\rho_{bh} = \left(\frac{0.23\ M_\odot}{\langle m_{bh} \rangle}\right)^{1/2} \rho_*(r) \tag{1.17}$$
$$\text{where } \rho_*(r) \equiv \frac{5}{16\pi} \frac{3 \times 10^6}{(1.8)^3} \left(\frac{r}{1.8}\right)^{-7/4}\ M_\odot\ \text{pc}^{-3}$$

provided that their assumption of the fraction of massive stars forming black holes is correct, and that energy is primarily lost from the cluster by black hole capture near the center. Only now has this theory been accompanied with observation of a collection of X-ray binaries observed within one parsec of the Galactic Center, possessing distinctive low-energy spectra that suggest these binaries are quiescent black hole low-mass X-ray binaries. Furthermore, their spatial distribution and luminosity function provide evidence for the existence of $\gtrsim 10,000$ additional isolated black holes (Hailey et al., 2018).

The aforementioned $M - \sigma$ relation predicts black holes of mass $10^2\ M_\odot < M_{\text{IMBH}} < 10^5\ M_\odot$ in smaller and fainter globular clusters, while various collapse scenarios also posit their existence in dense clusters. Gürkan et al. (2004) examined the possible dynamical evolution of young dense star clusters, and their N-body Monte Carlo simulations displayed rapid mass segregation and accelerated relaxation. Given that a Salpeter initial mass function is prone to the Spitzer instability (Spitzer Jr, 1969), i.e. the inability of heavier stars to establish energy equipartition with lighter stars, core collapse may occur within a fraction of both the relaxation time at the half mass radius and the timescale of massive star seg-

regation (see Eq. 1.8). If this timescale is less than the lifetime of massive stars, stars in the collapsing core can undergo a runaway collision process which produces a massive black hole of $\sim 0.1\%$ of the total cluster mass. Their work supports the findings of preceding smaller scale N-body simulations of stellar clusters (Zwart et al., 1998; Zwart & McMillan, 2002).

N-body codes simulating the dynamics of IMBHs in in-spiraling nuclear star clusters (NSCs) have depicted similar processes of mass segregation and accelerated relaxation. Focusing on the NSC in-fall formation scenario, in which dense massive clusters decay due to dynamical friction towards the center of the host galaxy and merge to form the central NSC (Tremaine et al., 1975), Mastrobuono-Battisti et al. (2014) modified N-body simulations as described in Antonini et al. (2012) to populate infalling clusters with IMBHs. Due to the IMBHs, the cluster relaxation time decreased by a factor of $\propto N_I M_I^2/(N_* M_*^2)$, with N_I and M_I being the number and mass of the IMBHs and N_* and M_* the number and mass of stars. The system's evolution is dominated by the two-body relaxation induced by the IMBHs, with the IMBHs' final density profile well-fitted to a power law $\rho_{\rm IMBH} \propto r^{-2.32}$. Note that is within the range expected for strong mass segregation ($2 \lesssim \alpha \lesssim 2.75$; see Alexander & Hopman, 2009), and although the density profile may be sensitive to significant statistical noise, the three simulations ran by Mastrobuono-Battisti et al. show consistent results indicating a clear cusp profile for the IMBHs when compared with the stellar core profile. The stellar component of the clusters formed a cusp early in the NSCs' evolution, with a slope slightly shallower than a Bahcall & Wolf slope ($\rho_* \propto r^{-1.26}$) and cusp radius of ~ 1 pc. Unlike the IMBHs, which interact and scatter but are never ejected from the system, the accelerated relaxation process increases the rate of stellar scattering and ejection.

Due to its proximity, the Galactic Center is a uniquely opportune environment to both study the dynamics of a stellar cluster dominated by a supermassive black hole, and search for stellar- and intermediate-mass black holes. With analysis of the stellar cluster population within 1 pc of Sgr A* showing a perplexing number of massive main-sequence stars (the so-called "paradox of youth"; see Ghez et al., 2003), various theories have been constructed that explain this observation by externalizing star formation. These theories hypothesize in-falling star cluster scenarios in which runaway formation of an IMBH can occur (see Gerhard, 2000; Kim & Morris, 2003; Zwart et al., 2003; McMillan & Zwart, 2003; Hansen & Milosavljević, 2003; Kim et al., 2004). Despite the plausibility of such hypotheses, there remains many predictions implied by resulting mass-segregation and ejection of low-mass stars which have not necessarily been observed in the Milky Way:

- a residual core, of which IRS 13E is a candidate (Schödel et al., 2005);
- a total cluster mass of $\gtrsim 10^5\ M_\odot$, which is an order of magnitude higher than observations;
- strong mass segregation and a loss of low mass stars at large radii. While there is no observed signature of mass segregation, there have been no detection of post-main sequence OB stars - stars experiencing high mass loss as they transition between Wolf-Rayet (WR) stars (Allen et al., 1990; Najarro et al., 1994, 1997) and extreme O supergiants (Morris et al., 1996) - beyond 0.5 pc.

The presence of higher mass objects may also be quantified by their effect on the motion of Sgr A*. Due to gravitational encounters with nearby objects, a massive black hole in a galaxy's center experiences a random walk in momentum space. The expected amplitude of this motion can be solved for with the mass of the black

hole $M_{\rm bh}$, the typical stellar mass $\langle m_* \rangle$, and the one-dimensional stellar velocity dispersion σ (Merritt et al., 2007; Chatterjee et al., 2002; Loeb & Furlanetto, 2013):

$$\begin{aligned} \langle V_{\rm bh}^2 \rangle &\approx 3\frac{\langle m_* \rangle}{M_{\rm bh}}\sigma^2 \\ &\approx 0.1 \text{ km s}^{-1} \left(\frac{\langle m_* \rangle}{M_\odot}\right) \left(\frac{M_{\rm bh}}{3\times10^6\ M_\odot}\right)^{-1} \left(\frac{\sigma}{100 \text{ km s}^{-1}}\right)^2 \end{aligned} \tag{1.18}$$

N-body simulations performed by Merritt et al. that ranged a variety of galaxy models and stellar masses demonstrated a proportion between Brownian velocity and black hole mass as $\langle V_{\rm bh}^2 \rangle \propto M_{\rm BH}^{-1/(3-\gamma)}$, where $0.5 \lesssim \gamma \lesssim 2.0$ represents the power-law index of the surrounding stellar density profile ($\rho \propto r^{-1}$). Using velocity dispersion data from Battaglia et al. (2005) and current mass estimates for Sgr A* (Gillessen et al., 2009; Ghez et al., 2008), we can derive an expected Brownian motion of $\langle V_{\rm Sgr}^2 \rangle \approx 0.2$ km s^{-1}. This prediction lies within constraints on the residual proper motion of Sgr A* perpendicular to the galaxy plane has been measured by Reid & Brunthaler (2004), though these measurements contain almost 1 km s^{-1} of uncertainty. Possible scenarios of a binary black hole with mass $\sim 10^3 - 10^5\ M_\odot$ in the Galactic Center, discussed by Hansen & Milosavljević (2003) and Yu & Tremaine (2003) to explain the existence of young stars and ejection of hypervelocity stars, are inherently restrained by limits on the velocity of Sgr A*. Current observations as well as the limits in IMBH mass outlined by Hansen & Milosavljević exclude IMBHs with masses greater than $\sim 10^4\ M_\odot$ and semimajor axes $\sim 10^3 - 10^5$ AU (~ 0.5 mpc $- 0.5$ pc), assuming accuracies of $0.1 - 1$ mas. We also have semi-major axis lower constraints due to gravitational wave timescales (Peters, 1964),

$$\begin{aligned} a &\geq 4\left(\frac{1}{5}\frac{G^3(M_{\rm Sgr}+M_{\rm IMBH})M_{\rm Sgr}M_{\rm IMBH}}{c^5}T_{\rm c}\right)^{1/4} \\ &\sim 0.7 \text{ mpc} \left(\frac{M_{\rm Sgr}}{4\times10^6\ M_\odot}\right)^{1/4} \left(\frac{M_{\rm IMBH}}{10^3\ M_\odot}\right)^{1/4} \left(\frac{T_c}{10^{10}\text{ yr}}\right)^{1/4}, \end{aligned} \tag{1.19}$$

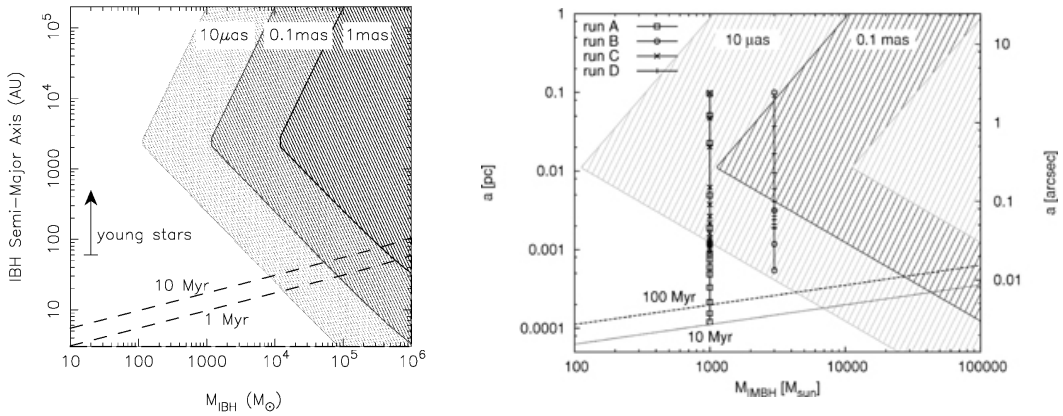

(a) Detection limits provided by Hansen & Milosavljević (2003)

(b) Detection limits provided by Löckmann & Baumgardt (2008), assuming a monitoring period of 10 yr.

Figure 1.1: Preliminary astrometric constraints on SMBH-IMBH binaries in the Galactic Center, assuming circular orbit, and SMBH mass of 3×10^6 $M_\odot$, and distance to Galactic Center as 8.5 kpc. Dotted lines represent coalescence due to gravitational wave radiation over various timescales.

such that the time of coalescence due to gravitational radiation (T_c) does not occur within Hubble time ($\sim$ 10 Gyr).

The short-term effects of IMBHs have also studied on the S2, which orbits Sgr A* at a semi-major axis of $\sim$ 5 milliparsecs (mpc) (Gillessen et al., 2009). Though general relativity produces perturbations on a time-scale of about 10 yr (Gillessen et al., 2009), a key signature of an IMBH in the vicinity of S2 would be a change in eccentricity and orbital plane of the star. An IMBH of mass greater than ~ 1000 $M_\odot$ at a distance of $\sim 1 - 5$ mpc may produce up to 1° shifts in the orbital plane per period (Gualandris et al., 2010).

The question remains, however, as to what extent the astrometric wobble of Sgr A* and orbital evolution of S2 can be accurately measured and used to infer a population of IMBHs in the Galactic Center. It is a complicated N-body problem that not only involves a central black hole and multiple IMBHs, but the stellar

population within the inner parsec of which the density profile is not well known. The predicted dynamical signature of an IMBH can be imitated by a population of mass-segregated objects (e.g. neutron stars, stellar-mass black holes). Alongside these potentially complicating factors is the small sphere of influence of an IMBH (using Eq.1.16 and fiducial measurements for globular clusters, $GM_{\rm BH}/\sigma^2 \approx 0.03$"), which makes data extremely sensitive to details of data-model comparison and lessens the statistical significance of IMBH detection (Van der Marel & Anderson, 2010; Baumgardt et al., 2002). Both numerically and observationally, determining a sufficient answer requires considerable accuracy.

1.4 Advancements in Astrometry

Fortunately, current advances in astrometry allow us to observe phenomena on a scale never before achieved. Through Very Long Baseline Interferometry (VLBI), astronomers may simultaneously observe a radio source with an array of radio telescopes, each of which intercepts the received signal to amplify, mix-down, and sample. The data is then correlated after accounting for the geometric delay, and produces an image with resolution inversely proportional to observing frequency ν and baseline B,

$$\theta_{\rm res} = \frac{c}{\nu B}$$

Since an array of N antennas acts as a collection of $N(N-1)/2$ paired interferometers, the maximum separation between a pair serves as a resolving baseline for the system. This has allowed for dramatic increases in the angular resolution of observations during the later 20th century, improving the first radio observations (Jansky, 1933, with order 10 degree error) by more than a factor of ten million ($\sim$ 0.001 arcsec currently). Millimeter wavelength VLBI (mm-VLBI) can be an

especially powerful though challenging technique to observe phenomena at angular resolutions unreachable elsewhere. While intrinsic problems such as atmospheric stability and induced fluctuations in signal phase grow more acute, these effects can be lessened if the overall sensitivity of the VLBI system is appropriately increased (e.g. through increasing bandwidth of observations or the rate at which data is sampled). mm-VLBI thus provides a great opportunity to discern more compact structures with impressive spatial resolution (For an in-depth review of VLBI, see Thompson et al., 2001; Kellermann & Moran, 2001; Middelberg & Bach, 2008).

In particular, we turn our attention to the Event Horizon Telescope (EHT) and GRAVITY. The EHT is an international collection of millimeter and submillimeter radio observatories, built to achieve an angular resolution comparable to the event horizon of Sgr A*. The EHT effectively creates an Earth-sized interferometer using telescopes stationed throughout the globe, and is capable of measuring relative positions and strengths within Sgr A* (e.g. accretion disk, jets) (Doeleman et al., 2008; Fish et al., 2011). Though the images produced do not alone translate to absolute positions due to lack of external phase reference, many of the VLBI stations incorporated in the EHT contain independent antennas that allow for simultaneous target sourcing and phase referencing. Hence, upon identifying a necessary phase-referencing candidate (e.g. a quasar), one can judiciously use antennas from various EHT stations to achieve micro-arcsecond (μas) scale astrometric positioning (see Broderick et al., 2011, for potential antenna configurations and reference sources). Similar to the EHT, GRAVITY can measure relative positions between a fringe tracking star and a source of interest as faint at $m_K \approx 17$ mag (Gillessen et al., 2010). In astrometric mode, GRAVITY reaches precisions of 10 μas by determining and tracking the centroid of an ob-

ject's emission (Eisenhauer et al., 2008). GRAVITY is additionally comprised of an optical/infrared telescope with $\sim$ 100 m diameter angular resolution and 200 m^2 collecting area, resolving between $2 - 140$ milliarcsecond features in imaging mode. The star S2 has already been observed by GRAVITY at 10s exposures for a total integration time of 300s, and these observations produced strong constraints on the magnitude of potential companions (see Abuter et al., 2017).

With this, both the EHT and GRAVITY will enable us to study the Galactic Center with unprecedented accuracy, endowing astronomers the ability to track the evolving position and velocity of S-stars and Sgr A*. Specifically, VLBI using various EHT stations with a necessary phase reference is best for accurately quantifying the evolving position and velocity of Sgr A*, while GRAVITY may be used to track the orbital dynamics of S2. Through this, we might in the future infer the existence of dark objects, their distribution, and the overall state of mass segregation. However, to obtain a preemptive idea on how this existence ultimately affects observations of Sgr A* and the S-star cluster, we rely on numerical simulations of this region.

1.5 Thesis Objective

The objective of this thesis is to determine whether, given a possible density profile for a black hole population in the inner parsec, their effect on the position of Sgr A* and the orbital parameters of S-stars is both detectable provided recent innovations in astrometry and differentiable from that of surrounding stars. Using modifiable density profiles informed by literature review for stellar- and intermediate-mass black holes, I developed a code that used the open-source *N*-

body integrator `REBOUND` (Rein & Liu, 2012) to create a simulated orbital system involving Sgr A*, a number of black holes, and the star S2. Through simulating scenarios in which the central parsec is populated and not populated with black holes, I identify the dynamical signature of these distinct and relatively larger-mass objects. This ultimately serves to establish additional hypothetical observational constraints and inform future EHT and GRAVITY data collections on the angular displacement of Sgr A* and evolving S-star orbits.

CHAPTER 2

PREVIOUS LIMITS

2.1 Constraints on Massive Binary Companions of Sgr A*

For over a decade, researchers have investigated the plausibility of detecting a single intermediate-mass black hole orbiting Sgr A* given current observational technologies and data on the proper motion of the central SMBH. To orient ourselves, let us consider the simple case of an SMBH - IMBH binary, with a primary and secondary mass m_1 and m_2 such that $m_1 \gg m_2$, separated by a distance r. For further simplicity, suppose the orbital plane is fully in our line of sight. We can calculate the distance of the center of the SMBH to the center of mass around which the SMBH "wobbles," as $a \equiv (rm_2/M)$ where $M = m_1 + m_2$, or approximately

$$a \approx \frac{rm_2}{m_1} = 2.5 \times 10^{-3} \text{ mpc} \left(\frac{r}{1 \text{ mpc}}\right) \left(\frac{m_2}{10^4 M_\odot}\right) \left(\frac{m_1}{4 \times 10^6 M_\odot}\right)^{-1} \tag{2.1}$$

From this, we can calculate the induced angular displacement of the SMBH as the angle $\Delta\theta$, which the length a subtends on the sky from a distance $R_0 \equiv 8.0$ kpc:

$$\Delta\theta \sim \frac{a}{R_0} \text{ rad} \tag{2.2}$$

$$\approx \frac{rm_2}{m_1 R_0} \frac{648000}{\pi} \text{ as} \tag{2.3}$$

$$= 25.8 \ \mu\text{as} \left(\frac{r}{1 \text{ mpc}}\right) \left(\frac{m_2}{10^4 M_\odot}\right) \left(\frac{m_1}{4 \times 10^6 M_\odot}\right)^{-1}$$

Note that while to date the Event Horizon Telescope (EHT) has achieved accuracies of ~ 60 μas with its baselines between Hawaii, California, and Arizona, it is projected that with the Atacama Large Millimeter Array (ALMA) the angular resolution of the array will double and future EHT observations could potentially resolve structures as fine as 15 μas.

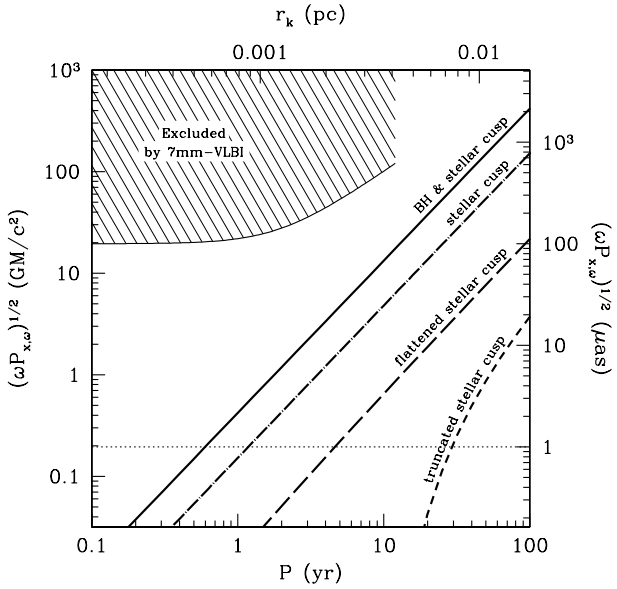

Figure 2.1: Power spectrum for the displacement of Sgr A* with surrounding stellar density profile (Schödel et al., 2007) and fiducial black hole density profile proportional to r^{-2}, estimated by Broderick et al. (2011)

This model however is clearly inadequate in describing an SMBH-IMBH binary in the Galactic Center, as it neglects whatever fluctuations are induced by surrounding environment of stars and stellar remnants. The stellar mass density within the inner parsec has been approximated by Schödel et al. (2007) as the broken power law:

$$\rho_*(r) \simeq (1.7 \pm 0.8) \times 10^6 \left(\frac{r}{0.22 \text{ pc}} \right)^{-\gamma} M_\odot \text{pc}^{-3} \tag{2.4}$$

where $\gamma = 1.2$ for $r < 0.22$ pc and $\gamma = 1.75$ for $r > 0.22$ pc. The mass density of stellar remnants is less constrained, though tens of thousands of stellar mass black holes are estimated to migrate towards the center and induce strong mass segregation (Miralda-Escudé & Gould, 2000; O'Leary et al., 2009; Alexander & Hopman, 2009). Broderick et al. (2011) approximate a power spectrum for the displacement of Sgr A*, assuming a stellar density profile described by Equation (2.4) and fiducial model for stellar black hole density, proportional to r^{-2}. They

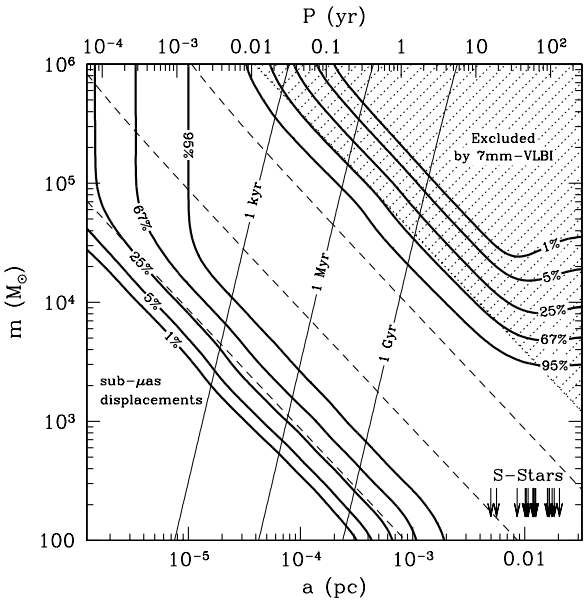

Figure 2.2: Estimated likelihood of SMBH-IMBH binaries to produce μas displacements of Sgr A* within a decade (Broderick et al., 2011)

found that in the most optimistic case of a stellar and black hole cusp, μas displacements occur on timescales of 0.5 years, while the most pessimistic case (which considers only a truncated stellar density extending up to 0.01 pc) produces μas displacements within a decade.

Given this additional Brownian noise, Broderick et al. (2011) adopted the two-body model of an SMBH-IMBH binary to estimate likelihoods of certain orbital parameters to induce μas deviations on sub-decade timescales, while necessarily satisfying already existing observational constraints. Sgr A* has already been subject to mm-VLBI observations, which have placed upper limits on the velocity component perpendicular to the galactic plane at -0.4 ± 0.9 km s^{-1} (Reid & Brunthaler, 2004). Uncertainties on this values may be attributed to galactic precession or the position wander of referenced extragalactic radio sources (see Hosokawa et al., 2002), alongside the presently limited accuracy of radio observations. 7mm proper motion studies have additionally failed to find evidence for

oscillatory signals with periodicities within $\sim$ 20 yr (Reid et al., 1999; Reid & Brunthaler, 2004). Broderick et al. found that this model, when considering circular orbits with periods comparable to observation timescales, rules out companion masses with an associated semi-major axis a

$$M_{\rm IMBH} \gtrsim 8 \times 10^4 \left(\frac{a}{0.48 \text{ mpc}} \right)^{-1} M_\odot \tag{2.5}$$

Reid & Brunthaler (2004) provide additional limits on a possible binary black hole in the Galactic Center, based on proper motion estimates for Sgr A*. They found that with given proper motion measurements, we can roughly exclude IMBHs of mass $\gtrsim 10^4$ $M_\odot$ and semi-major axes of $10^3 - 10^5$ AU.

2.2 IMBHs as Perturbers of Stellar Orbits

Key to much of our understanding of the properties of Sgr A* have been the S-stars, which orbit within the inner most arcsecond. Their orbital dynamics overwhelmingly support the existence of a single point mass of $\sim 4 \times 10^6$ $M_\odot$ at a distance $\sim$ 8 kpc, providing some of the most conclusive evidence that Sgr A* is in fact a supermassive black hole (Gillessen et al., 2009) . A thoroughly examined S-star has been S2, which possesses an orbit of $\sim$ 16 yr and has been most frequently used to estimate the mass of Sgr A*. While the S-stars are all modeled by Keplerian orbits, S2 provides the best opportunity to potentially observe deviations associated with relativistic effects or the presence of dark stellar remnants given its relative brightness.

Being young stars in an environment that hinders star formation, the S-stars have been the subjects of infalling star cluster models in which an IMBH is a necessary transport vehicle (Hansen & Milosavljević, 2003; Zwart et al., 2003;

Freitag et al., 2006). Additionally, the random orientation of the S-star orbits and distribution of eccentricities have been reproduced in numerical simulations of Myr-long interactions between the S-stars and an IMBH of mass $\gtrsim 1.5 \times 10^3\ M_\odot$ (Merritt et al., 2009; Perets et al., 2009; Gualandris & Merritt, 2009). The presence of an IMBH near the S-stars has been theoretically constrained, with Mikkola & Merritt (2008) demonstrating that an IMBH of mass $\sim 10^{-3}\ M_{\rm Sgr}$ orbiting at a distance of 1 mpc would destabilize the S-star system, and Gillessen et al. (2010) concluding that the phase space of S2 implies that no mass larger than $0.02 M_{\rm Sgr}$ can exist within its orbit.

Gualandris et al. (2010) investigated the short term effects that an IMBH may have on the star S2 with N-body simulations and orbital fitting techniques, taking into account non-trivial effects induced by general relativity. They consider a three-body model in which the IMBH and S2 are placed in Keplerian orbits around the central SMBH, and record the evolution of the orbital parameters of S2 over 50 years (during which the star completes three full orbits). In such a short timescale, effects of other S-stars are negligible and any variation can be attributed to the IMBH; oscillations potentially indicative of Kozai mechanisms (Kozai, 1962) are also irrelevant, as in each simulated scenario the periods of these mechanisms exceed other (namely GR) precession timescales. For masses $M_{\rm IMBH} \gtrsim 2000\ M_\odot$ and semi-major axes $a \lesssim 3$ mpc, an IMBH induces on average over one orbit a shift in apoapsis greater than the estimated relativistic shift of ~ 0.83 mas. Such is a distinguishable signature on the angular momentum (eccentricity and orbital plane) of S2, potentially observable once S2 returns to its periapse. Gualandris et al. additionally estimated the detectability of an IMBH perturbing S2, fitting their simulated data sets with the same code as Gillessen et al. (2009) to construct the full set of parameters describing the orbit of S2 and gravitational potential of

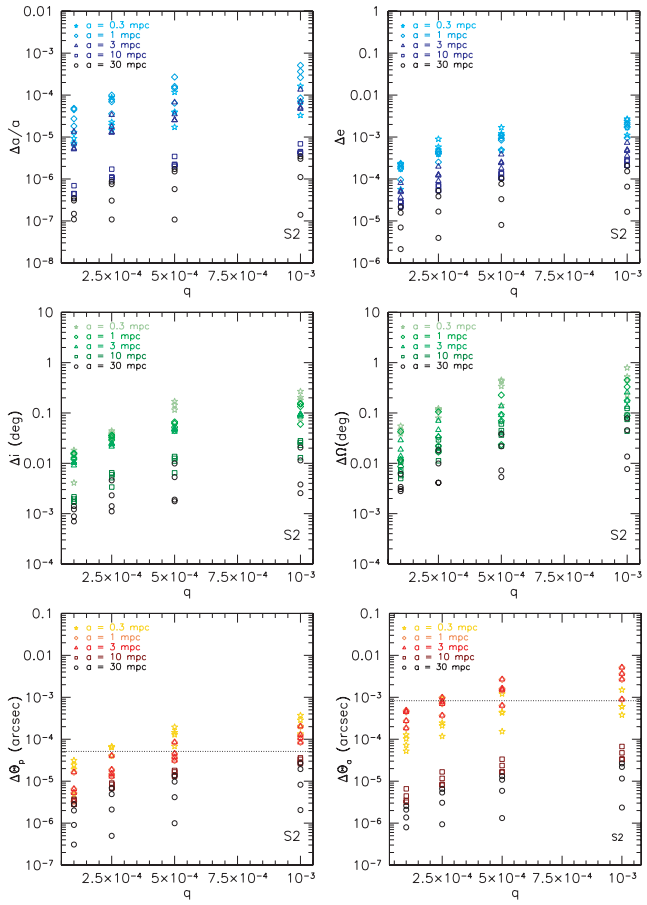

(a) Average changes of the orbital elements (semi-major axis, eccentricity, inclination, position angle of ascending node, periapse, and apoapse) of S2 in a full orbit versus the mass ratio $q \equiv M_{\rm IMBH}/M_{\rm SMBH}$ in simulations performed by Gualandris et al. (2010). Dotted lines represent GR shift in periapse and apoapse.

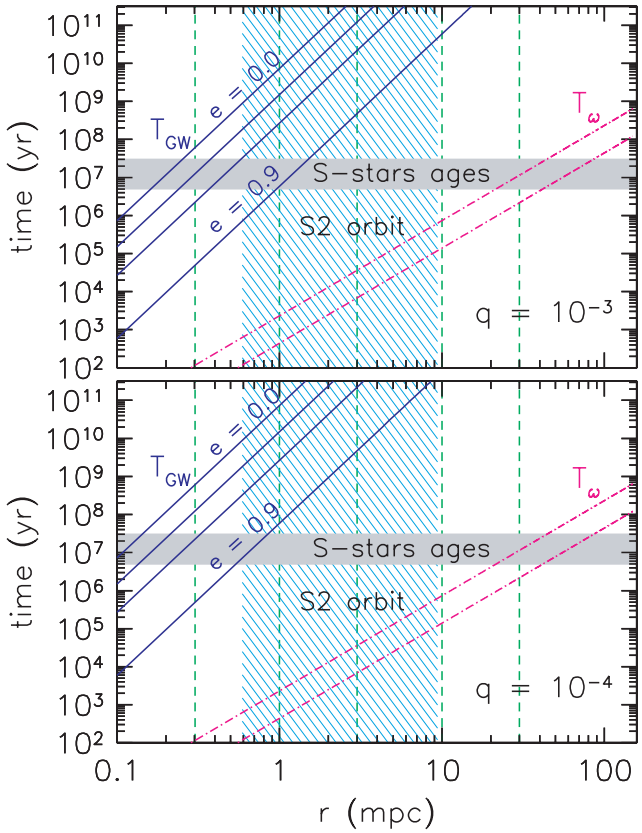

(b) Time-scales associated with the orbital evolution in simulations performed by Gualandris et al. (2010). Solid lines represent GW time-scale for a black hole binary with $q \equiv M_{\rm IMBH}/M_{\rm SMBH} = 10^{-4}$ (top panel) and $q = 10^{-3}$ (bottom panel), for eccentricities $e = 0, 0.5, 0.7, 0.9$. Dot-dashed lines represent GR precession time-scale for $e = 0$ (upper pink line) and $e = 0.9$ (lower pink line). Vertical green dotted lines represent adopted value for initial semi-major axis of the binary.

Figure 2.3: Time-scales and results of a N-body simulations performed by Gualandris et al. (2010), studying the effects of a single IMBH on the orbit of the star S2.

the SMBH. Data that did not adequately fit the relativistic equations of motion were identified as reflecting discernible IMBH perturbations. For IMBH masses of 400 $M_{\odot}$, 10^3 $M_{\odot}$, 2×10^3 $M_{\odot}$, and 4×10^3 $M_{\odot}$, the percentage of detectable IMBHs are 15, 39, 51, and 66 per cent, respectively.

2.3 Tentative Conclusions

From the literature we find that considerable important work has been performed on estimating and constraining the existence of a single IMBH in the Galactic Center. However, various theories postulate the existence of a *population* of IMBHs as opposed to just one, meaning that it is imperative that we estimate dynamical signatures that reflect the presence of a number of massive dark objects. The following chapter will describe models for these populations that are analyzed in this work, along with the numerical methods used to investigate their possible cumulative effect on the position of Sgr A* and orbit of S2.

CHAPTER 3

METHODS

3.1 Theoretical Models

3.1.1 Surrounding Stellar Population

In this work, I consider a central black hole with mass $M_{\rm cbh} = 4.4 \times 10^6\ M_\odot$ within a stellar cluster described by a Hernquist (1990) spherical density profile

$$\rho_{\rm H}(r) = \frac{M_{\rm c}}{2\pi}\frac{a}{r(r+a)^3} \tag{3.1}$$

where $M_{\rm c} = 4.4 \times 10^6\ M_\odot$ is the total cluster mass, and $a = 1$ pc the scale length. In the treatment outlined by Tremaine et al. (1994), the Hernquist model is a special case in a family of spherical stellar models with a similar outer density profile $\rho \propto r^{-4}$ and central density cusp $\rho \propto r^{\eta-3}$ $(0 < \eta \leq 3)$, corresponding to $\eta = 2$. I adopt a Hernquist profile defined by the above set of parameters as a relatively close approximation to the actual broken law stellar density in the inner parsec (see Equation (2.4)).

The cumulative mass of the stellar cluster contained within a radius r is calculated through an integration of the above density profile:

$$\begin{aligned} M_{\rm H}(<r) &= \int_0^r 4\pi s^2 \rho_{\rm H}(s) ds \\ &= \frac{M_{\rm c} r^2}{(r+a)^2} \end{aligned} \tag{3.2}$$

inducing a gravitational acceleration $\mathbf{a}$ and potential Φ on an object with position

vector $\mathbf{r}$:

$$\begin{aligned}\mathbf{a}_{\mathrm{H}}(\mathbf{r}) &= -\frac{GM_{\mathrm{H}}(<r)}{r^2}\hat{\mathbf{r}} \\ &= -\frac{GM_{\mathrm{c}}}{(a+r)^2}\hat{\mathbf{r}} \qquad (3.3)\\ \Phi_{\mathrm{H}}(\mathbf{r}) &= \int_r^\infty \mathbf{a}_{\mathrm{H}}(\mathbf{s})\cdot d\mathbf{s} \\ &= \int_r^\infty -\frac{GM_{\mathrm{c}}}{(a+s)^2}\hat{\mathbf{s}}\cdot d\mathbf{s} \\ &= -\frac{GM_{\mathrm{c}}}{a+r} \qquad (3.4)\end{aligned}$$

Tremaine et al. provide an explicit phase space distribution function in terms of energy per unit mass, assuming natural units where $G = M_{\mathrm{c}} = a = 1$ and mass ratio $\mu = M_{\mathrm{BH}}/M_{\mathrm{c}}$:

$$f_1(\mathcal{E}) = \frac{2\Gamma(2)}{2^{7/2}\pi^{5/2}\mu\Gamma(\frac{3}{2})}\mathcal{E}^{-1/2} \qquad (3.5)$$

For any standard units of length, mass and time, Equation (3.5) becomes:

$$f_1(\mathcal{E}) = \frac{2\Gamma(2)}{2^{7/2}\pi^{5/2}(GM_{\mathrm{c}}a)^{3/2}\mu\Gamma(\frac{3}{2})}\mathcal{E}^{-1/2} \qquad (3.6)$$

3.1.2 Stellar Mass Black Holes

In defining a test density profile for black holes of characteristic mass 10 $M_\odot$ and 100 $M_\odot$, I adapt the methods of Miralda-Escudé & Gould (2000) to reflect new understandings of the stellar density profile in the inner parsec. Miralda-Escudé & Gould follow Bailyn et al. (1998) by supposing that ordinary stars of mass $\gtrsim 30\ M_\odot$ in the galactic bulge will undergo core collapse and form black holes of mass $\lesssim 7\ M_\odot$. Since the stellar mass black holes form from an already existing system of stars, Miralda-Escudé & Gould constructed a density profile that is necessarily a fraction of that of the stellar cluster, determined according to the

Salpeter (1955) initial mass function. Given a characteristic black hole mass $M_{\rm BH}$ and stellar density profile $\rho_*(r)$:

$$\rho_{\rm SBH}(r) = C\rho_*(r),\ C \equiv \left(\frac{0.23\ M_\odot}{\langle M_{\rm BH}\rangle}\right)^{\frac{1}{2}} \tag{3.7}$$

To be self-consistent, I suppose the surrounding stellar system is described by a Hernquist profile and set $\rho_*(r) = \rho_{\rm H}(r)$ (see Equation (3.1)). Two distinct stellar black hole density profiles are defined by considering $\langle M_{\rm BH}\rangle$ as 10 $M_\odot$ and 100 $M_\odot$. With this definition, the mass contained within a certain radius, acceleration, and potential according to this stellar black hole density profile is proportional to that of the stellar Hernquist profile:

$$\begin{aligned} M_{\rm SBH}(<r) &= C\ M_{\rm H}(<r) \\ &= C\frac{M_{\rm c}r^2}{(r+a)^2} \end{aligned} \tag{3.8}$$

$$\begin{aligned} \mathbf{a}_{\rm SBH}(\mathbf{r}) &= C\ \mathbf{a}_{\rm H}(\mathbf{r}) \\ &= -\frac{CGM_{\rm c}}{(a+r)^2}\hat{\mathbf{r}} \end{aligned} \tag{3.9}$$

$$\begin{aligned} \Phi_{\rm SBH}(\mathbf{r}) &= C\ \Phi_{\rm H}(\mathbf{r}) \\ &= -\frac{CGM_{\rm c}}{a+r}\hat{\mathbf{r}}. \end{aligned} \tag{3.10}$$

3.1.3 Intermediate Mass Black Holes

This work is particularly concerned with IMBH density profiles of characteristic mass $10^3\ M_\odot$ and $10^4\ M_\odot$, informed the results of theoretical simulations studying the formation and evolution of infalling cluster systems. From the literature I have selected two density profiles to investigate, both of which are of the form

$$\rho_{\rm IMBH}(r) = \rho_0\left(\frac{r}{r_0}\right)^{-\gamma} \tag{3.11}$$

Appendix A offers an in-depth calculation and solution of the enclosed mass, acceleration, and gravitational potential associated with this generalized density profile. As this density profile diverges as r approaches 0, an inner cut-off radius is defined as the semi-major axis a_c associated with a gravitational wave time of coalescence equaling 10 Gyr. (See Equation (1.19)).

For IMBHs of mass $\sim 1000\ M_\odot$, Zwart et al. (2006) predict that ~ 50 will be present within 10 pc of Sgr A*. They provide no explicit density profile, though general predictions of the final mass-segregated distribution of stellar remnants range from flat-cores to extreme cusps (Alexander & Hopman, 2009; Merritt, 2010, e.g). With this in mind I adopt a fiducial $\rho \propto r^{-2}$ model (otherwise known as the isothermal sphere) to fit the estimated number of $\sim 1000\ M_\odot$ IMBHs provided by Zwart et al.:

$$\rho_{\mathrm{Z06}}(r) = \frac{5.0 \times 10^3}{4\pi} \left(\frac{r}{\mathrm{pc}}\right)^{-2}\ M_\odot \mathrm{pc}^{-3} \tag{3.12}$$

This possesses the following enclosed mass, acceleration, and potential:

$$M_{\mathrm{Z06}}(< r) = 5.0 \times 10^3\ M_\odot \left(\frac{r}{\mathrm{pc}}\right), \tag{3.13}$$

$$\mathbf{a}_{\mathrm{Z06}}(\mathbf{r}) = -6.86 \times 10^7\ \frac{\mathrm{cm}}{\mathrm{s}^2} \left(\frac{r}{\mathrm{pc}}\right)^{-1} \hat{\mathbf{r}}, \tag{3.14}$$

$$\Phi_{\mathrm{Z06}}(\mathbf{r}) = -2.12 \times 10^{12} \left[\ln\left(\frac{r}{\mathrm{pc}}\right) + 42.6\right]\ \mathrm{erg} \tag{3.15}$$

Note that according to $M_{\mathrm{Z06}}(< r)$, the nearest $1000\ M_\odot$ IMBH would be approximately 0.2 pc from the center.

For IMBHs of mass $\sim\ 10^4\ M_\odot$, I consider the density profile obtained by Mastrobuono-Battisti et al. (2014) in their work simulating twelve in-spiraling nuclear star clusters:

$$\rho_{\mathrm{M14}}(r) = 6.20 \times 10^3 \left(\frac{r}{\mathrm{pc}}\right)^{-2.32}\ M_\odot \mathrm{pc}^{-3} \tag{3.16}$$

From the density profile, I may calculate the enclosed mass, gravitational acceleration, and potential as

$$M_{\rm M14}(<r) = 1.15 \times 10^5 \ M_\odot \left(\frac{r}{\rm pc}\right)^{0.68}, \tag{3.17}$$

$$\mathbf{a}_{\rm M14}(\mathbf{r}) = -1.60 \times 10^6 \ \frac{\rm cm}{\rm s^2} \left(\frac{r}{\rm pc}\right)^{-1.32} \hat{\mathbf{r}}, \tag{3.18}$$

$$\Phi_{\rm M14}(\mathbf{r}) = -1.54 \times 10^{13} \left(\frac{r}{\rm pc}\right)^{-0.32} \ {\rm erg} \tag{3.19}$$

3.1.4 Orbital Parameters for S2

The Keplerian orbit of S2 and other S-stars have been fitted by Gillessen et al. (2009) to describe six parameters: semi major axis a, eccentricity e, inclination i, angle of the line of nodes Ω, angle from ascending node to pericenter ω, and the time of pericenter passage t_P. They implement various relativistic effects into the orbital fitting routine and marked the position of the center of mass by the near infrared flares of Sgr A* (see Genzel et al., 2003), following standard procedures of χ^2 fit (Press et al., 1994) to calculate statistical errors. I include parameters for two of the other brightest S-stars beyond S2 in Table 3.1, as structure of the simulation code (see Section 3.2) is such that one could input the parameters of any S-star into the simulated orbital system and investigate the short-term effects of a black hole population on its orbit.

3.2 Simulation Structure

To model and simulate an orbital system involving a variable black hole density profile, I developed a `Python` package using the open-source, multi-purpose N-body

Star	a["]	e	i [°]	Ω [°]	ω [°]	t_P [yr-2000]
S1	0.508±0.028	0.496±0.028	120.82±0.46	341.61±0.51	115.3±2.5	0.95±0.27
S2	0.123±0.001	0.880±0.003	135.25±0.47	225.39±0.84	63.56±0.84	2.32±0.01
S8	0.411±0.004	0.824±0.014	74.01±0.73	315.90±0.50	345.2±1.1	-16.2±0.4

Table 3.1: Examples of Keplerian fits made by Gillessen et al. (2009) for the S-stars, which orbit in the inner arc second of the galactic center. For this work, I examine the effects produced on Keplerian elements of S2.

software package `REBOUND` Rein & Liu (2012). `REBOUND` is designed to integrate a variety of gravitational systems and supporting both collisional and collision-less (classical) dynamics; upon importing the package simulations may be initialized and performed via a provisional `Python` module. The `Python` package created for the purposes of this work used `REBOUND` to randomly realize and integrate two types of orbital systems: (1) Sgr A* and S2 along with varied IMBH/stellar populations, and (2) Sgr A* and S2 affected by a *smooth* density profile matching those of the varied IMBH populations. This is differentiated to investigate whether the effects of discrete objects on the orbital parameters of S2 are significantly different from a smoothly distributed mass. To numerically solve the corresponding equations of motion, I use the integrator `Mercurius`, a hybrid integration scheme provided by `REBOUND` and developed by its creators (Rein & Spiegel, 2014; Rein & Tamayo, 2015). For an explanation and discussion of numerical methods, see Section 3.3. Error is kept at a minimum by identifying the optimal time step for each simulated scenario, which ranged from 20 hours to 80 hours.

To initialize the program, I place at the origin a resting SMBH of mass $M_{\rm SMBH} = 4.4 \times 10^6\ M_\odot$, along with the star S2 described by its mass and orbital parameters. These act as the only active particles of the simulation; all other added particles are treated as semi-active, gravitationally interacting with the central massive object and the S-star, but not with each other. The properties of the

integrator are further set such that the simulation merges particles that collide with each other, preserving mass and momentum, and tracks energy that is lost due to collisions. Based on the density profile being simulated, I determine an outer-most distance at which we draw remaining particles. For stellar and intermediate mass black holes, this distance was set as $r_{\rm max} = 1.0$ pc. For the stellar control, this was 0.1 pc. Similarly, an inner-most distance is calculated to mark the absolute closest distance from Sgr A* an orbiting objects may be. For stellar and intermediate-mass black holes, this is constrained by their gravitational wave timescale (Peters, 1964, or Equation (1.19)), and for stars, this is their tidal radius (Equation (1.13)).

To randomly distribute particles of mass m with a density profile ρ, I first calculate the number present in the simulation as

$$N_{\rm p} = \frac{1}{m} \int_{r_{\rm min}}^{r_{\rm max}} M_\rho(r) dr \tag{3.20}$$

where $M_\rho(r)$ describes the total mass contained within a radius r. The actual number of distributed particles is determined by drawing from a Poisson distribution with $N_{\rm p}$ as the mean. The distance of each particle from the origin is then obtained through an inverse transform sampling method, with $f(r) = M(r)/(M_{\rm tot})$ serving as the cumulative density function (CDF) for particle position. In this method, I uniformly draw a value u from the interval $(f(r_{\rm min}), f(r_{\rm max})) \subset [0, 1]$, let $m_u = M_{\rm tot} * u$, and calculate the particle position as $r = f^{-1}(m_u)$. The unit directional vector $\hat{\mathbf{r}} = (x, y, z)$ of the particle position is then determined via sphere point picking: given random variate $u \in [-1, 1]$ and $\theta \in [0, 2\pi)$,

$$x = \sqrt{1 - u^2} \cos\theta \tag{3.21}$$

$$y = \sqrt{1 - u^2} \sin\theta \tag{3.22}$$

$$z = u \tag{3.23}$$

For each particle at a known position $\mathbf{r}$, the phase space distribution of the orbital system – estimated as (3.5) – depends only on velocity. One can approximate then that within a sufficiently thin enough spherical shell, centered at that radius, there exists a similar dependency. As such, I inversely derive a CDF describing the distribution of bound velocities ($v < \sqrt{-2\Phi}$) for approximately 1000 spherical shells of thickness $10^{-3}\ r_{\max}$ situated between $r_{\min}$ and $r_{\max}$. Given a position $\mathbf{r}$ for a particle, I determine what spherical shell it falls into to calculate the appropriate velocity CDF. The particle speed is then randomly drawn from this CDF through the inverse transform sampling method. Upon drawing this magnitude, the direction of the velocity vector is randomly determined and ensured to be perpendicular to the position vector.

Having determined the position and velocity vectors for each particle, I calculate the following orbital elements and add the particles with said elements specified to the orbital simulation:

- Semi-major axis: $a = \dfrac{GM_{\text{cbh}}r}{2GM_{\text{cbh}} - v^2 r}$
- Eccentricity: $e = |\mathbf{e}| = \left|\dfrac{\mathbf{v}\times\mathbf{h}}{GM_{\text{cbh}}} - \dfrac{\mathbf{r}}{r}\right|$, $\mathbf{h} \equiv \mathbf{r}\times\mathbf{v}$
- Inclination: $i = \arccos\left(\dfrac{h_z}{|\mathbf{h}|}\right)$
- Longitude of ascending node: $\Omega = \begin{cases} \arccos\left(\dfrac{n_x}{|\mathbf{n}|}\right), & n_y \geq 0 \\ 2\pi - \arccos\left(\dfrac{n_x}{|\mathbf{n}|}\right), & n_y < 0 \end{cases}$,

  $\mathbf{n} \equiv (-h_y, h_x, 0)$
- Argument of periapses: $\omega = \arccos\left(\dfrac{\mathbf{n}\cdot\mathbf{e}}{|\mathbf{n}||\mathbf{e}|}\right)$
- True anomaly: $\nu = \arccos\left(\dfrac{\mathbf{e}\cdot\mathbf{r}}{|\mathbf{e}||\mathbf{r}|}\right)$

For simulations testing the effects of smooth (as opposed to discrete) density profiles, I do not add any other particles besides Sgr A* and S2. Instead, I define an additional force emulating the acceleration induced by the density profile in question. No additional significant dynamical or velocity-dependent forces are incorporated into the simulation due to the short length of the integration.

For each density profile, I performed 1500 different random realizations of the associated particle system surrounding Sgr A* and S2. All simulations were integrated to an end-time of 16 yr, passing a list of 10000 output times. Between each call of the integration method, I record the position and velocity Cartesian components of Sgr A* and S2, the various orbital elements of S2 (a, e, i, Ω, and ω), and the total number of particles remaining in the simulation. Relative energy error was calculated, and simulations reaching relative energy errors greater than 10^{-7} (1×10^{-4} for stellar control) were discarded from the analyzed dataset.

3.3 Numerical Algorithms

These simulations use the hybrid symplectic integrator `Mercurius`, which combines the `WHFast` and `IAS15` integrator modules already built into `REBOUND`. Traditionally, symplectic integrators are ideal for integrations of orbital systems as they conserve necessary invariants such as phase-space density. However, they are significantly less capable of maintaining such quantities when the time step is adaptive to close encounters (Gladman et al., 1991; Hairer et al., 2006) or when particles experience non-conservative forces. `Mercurius` works similarly to the `MERCURY` package (Chambers, 1999) by switching to a non-symplectic algorithm during close encounters, allowing the integrator to adaptively reduce the step-size

while maintaining a similar level of accuracy. Below is a review of symplectic theory, along with an explanation of the `WHFast` and `IAS15` algorithms.

3.3.1 Theory of Symplectic Integrators

Generally, the orbits of objects within a system dominated by a massive central body are regarded as weakly perturbed Keplerian orbits. Thus, for long-term integrations researchers often adopt schemes which are designed to numerically solve slightly perturbed Hamiltonian systems while better conserving quantities like energy or angular momentum.

The notion of symplecticity arises from such efforts. Consider a system of n particles, with $\Omega \subset \mathbb{R}^{2n}$ corresponding to the phase space of the system. An element of Ω is denoted as $(\mathbf{q}, \mathbf{p})$, where $\mathbf{q}$ and $\mathbf{p}$ consist of n components indexing the position and momentum of each particle respectively. We say Ω possesses a *symplectic* structure if there exists some mapping $\omega : \Omega \times \Omega \to \mathbb{R}$ that is

- *bilinear*: $\omega(\sum_{i=0}^{n} a_i \mathbf{u}_i, \sum_{j=0}^{n} b_j \mathbf{v}_j) = \sum_{j=0}^{n} \sum_{i=0}^{n} a_i b_j \omega(\mathbf{u}_i, \mathbf{v}_j)$ for all $\mathbf{u}_i, \mathbf{v}_j \in \Omega$ and $a_i, b_i \in \mathbb{R}$,
- *alternating*: $\omega(\mathbf{v}, \mathbf{v}) = 0$ for all $\mathbf{v} \in \Omega$,
- and *non-degenerate*: If $\omega(\mathbf{u}, \mathbf{v}) = 0$ for all $\mathbf{v} \in \Omega$, then $\mathbf{u} = 0$.

We can define a symplectic bilinear form $\omega = \sum_{i=1}^{n} dq_i \wedge dp_i$, where $dq_i \wedge dp_i$ is a differential two-form defined as

$$dq_i \wedge dp_i : \Omega \times \Omega \to \mathbb{R} \qquad ((\mathbf{q}_1, \mathbf{p}_1), (\mathbf{q}_2, \mathbf{p}_2)) \mapsto q_{1i} p_{2i} - q_{2i} p_{1i} \tag{3.24}$$

A smooth complex function $H \in C^\infty(\Omega)$ gives rise to a Hamiltonian system of ordinary differential equations:

$$\dot{q}_i = \frac{\partial H}{\partial p_i} \qquad \dot{p}_i = -\frac{\partial H}{\partial q_i} \tag{3.25}$$

Liouville's theorem states that the time evolution of the Hamiltonian is a volume-preserving transformation of phase space, meaning that the phase space volume occupied by a system evolving in accordance to Hamilton's equations of motion will remain constant through time. This requires that the exact solutions of Hamiltonian equations of motion conserve energy and preserve the underlying symplectic form: supposing $(\widetilde{\mathbf{q}}, \widetilde{\mathbf{p}}')$ are the transformed coordinates of $(\mathbf{q}, \mathbf{p})$ from $t = 0$ to $t = \tau$, $\sum dq_i \wedge dp_i = \sum d\widetilde{q}_i \wedge d\widetilde{p}_i$ and $H(q,p) = H(\widetilde{q}, \widetilde{p})$. One would naturally seek, then, a numerical integrator that conserves H and $dq \wedge dp$ at each time step; however such an integration scheme cannot exist for non-integrable Hamiltonian systems (Ge & Marsden, 1988). Thus, we require a compromise: a symplectic integrator that conserves the symplectic structure provided by $dq \wedge dp$.

Ruth (1983) first developed an explicit symplectic scheme for separable Hamiltonians of the form $H = T(\mathbf{p}) + V(\mathbf{q})$. One can construct an n-th order explicit symplectic integrator which approximates the original Hamiltonian flow by repeatedly composing symplectic mappings $(q,p) \mapsto (q',p')$:

$$q' = q + c_i \tau \left(\frac{\partial T}{\partial p} \right), \; p' = p \tag{3.26}$$

and

$$q' = q, \; p' = p - d_i \tau \left(\frac{\partial V}{\partial q} \right) \tag{3.27}$$

The numerical coefficients c_i, d_i are determined such that the resulting mapping reflects a Taylor expansion of the solution to the Hamiltonian, up to order τ^n. In

fact, the first order symplectic mapping ($c_i = d_i = 1$) exactly describes the time-τ evolution of a slightly perturbed Hamiltonian

$$\widetilde{H} = H + \tau H_1 + \tau^2 H_2 + \cdots \tag{3.28}$$

where $H = T(\mathbf{p}) + V(\mathbf{q})$ is our original Hamiltonian and

$$H_1 = \frac{1}{2} H_p H_q,\ H_2 = \frac{1}{12}(H_{pp} H_q^2 + H_{qq} H_p^2),\ H_3 = \frac{1}{12} H_{pp} H_{qq} H_p H_2, \ldots \tag{3.29}$$

(see Dragt & Finn, 1976; Dragt et al., 1988, for in-depth proof and discussion.).

A more generalized symplectic mapping method, first devised by Wisdom (1982, 1983) and properly formulated by Wisdom & Holman (1991), exploits the commonly referred to averaging principle of Lagrange and Laplace. In this principle Lagrange and Laplace argue that, over a long period of time, rapidly oscillating terms average out and provide no net effect on a system's evolution; significant evolutionary contributions accrue from secular terms (see Moulton, 2012, for historical review). Traditional integration schemes relied on this principle to justify averaging over or removing high frequency oscillations from the averaged equations of motion to reach approximate solutions (e.g. Schubart, 1964, 1968). Wisdom and Holman realized that, at the same level of accuracy, one can selectively add high-frequency terms to construct a fully integrable Hamiltonian that closely approximates the original. Inspired by Chirikov (1979), they chose rapidly oscillating terms that sum to trivially integrable periodic delta functions; for example, letting H be an unperturbed and integrable Hamiltonian and $\widetilde{H} = H - \mathbf{H}'$ the perturbed Hamiltonian in question, a second-order mapping corresponding to $\widetilde{H}$ is

$$H_{map} = H - 2\pi\delta_{2\pi}(\Omega t - \pi)(\mathbf{H}') \tag{3.30}$$

where $\delta_{2\pi}(x)$ is a periodic delta function with period 2π, Δt is the integration time step, and $\Omega = 2\pi/\Delta t$ is the mapping frequency.

3.3.2 `WHFast` Algorithm

The `REBOUND` Wisdom-Holman integrator is a re-implementation of the Wisdom-Holman method that significantly improves the Kepler solver and numerical stability of transformations between Cartesian and Jacobi coordinates. `WHFast` functions by re-writing the Hamiltonian of a system with Jacobi coordinates to separate it into easily integrable parts. For a system of N particles, we can write the Hamiltonian as the sum of three terms using conjugate mass and momentum:

$$H = H_0 + H_\mathrm{K} + H_\mathrm{I} \tag{3.31}$$

where

$$\begin{aligned}
H_0 &= \frac{\mathbf{p}_0'^2}{2m_0'}, \\
H_\mathrm{K} &= \sum_{i=1}^{N-1} \frac{\mathbf{p}_i'}{2m_i'} - \sum_{i=1}^{N-1} \frac{Gm_i'M_i}{|\mathbf{r}_i'|}, \text{ and} \\
H_\mathrm{I} &= \sum_{i=1}^{N-1} \frac{Gm_i'M_i}{,} |\mathbf{r}_i'| - \sum_{i=0}^{N-1} \sum_{j=i+1}^{N-1} \frac{Gm_im_j}{|\mathbf{r}_i - \mathbf{r}_j|} \\
m_i' &\equiv \frac{m_iM_{i-1}}{m_i + M_{i-1}}, \; M_i \equiv \sum_{j=0}^{i} m_j, \\
\mathbf{p}_i' &\equiv m_i'\mathbf{v}_i', \; \mathbf{v}_i' \equiv \mathbf{v}_i - \frac{1}{M_{i-1}} \sum_{j=0}^{i-1} m_j\dot{\mathbf{r}}_j
\end{aligned} \tag{3.32}$$

H_0 describes the motion of the center of mass ($\mathbf{r}_0'$) along a straight line, which allows the system to integrate particles with respect to any inertial frame of reference. The ith term of H_K reflects the Keplerian motion of the ith particle around the center of mass of all interior particles. H_I accounts for the interactions between each of the particles. H_0 and H_I already possess analytical solutions, while H_K can be iteratively solved. The symplectic integrator is then constructed for the total Hamiltonian using the operator split method in Jacobi and Cartesian coordinates (see Saha & Tremaine, 1992). Denoting the evolution of particles under a

Hamiltonian H for a time dt by the operator $\hat{H}(dt)$, the system evolves under the Drift-Kick-Drift scheme, also referred to as the Wisdom-Holman map:

Step 1 (Drift): Apply $\hat{H}_{\mathrm{K}}(dt/2) \circ \hat{H}_0(dt/2)$

Step 2 (Kick): Apply $\hat{H}_{\mathrm{I}}(dt)$

Step 3 (Drift): Apply $\hat{H}_{\mathrm{K}}(dt/2) \circ \hat{H}_0(dt/2)$

As long as H_{K} and H_0 commute, the ordering of the first and last step do not matter and can be combined if the system is evolved for multiple time steps. To adjust for the relatively large short-term oscillations that symplectic integrators induce, `WHFast` also implements by default an 11th-order symplectic corrector. For a full derivation of symplectic correctors, see Wisdom et al. (1996) and Mikkola & Palmer (2000).

3.3.3 `IAS15` Algorithm

`IAS15`, alternatively, is a non-symplectic approach to orbital integration. It is a 15th order implicit integrator with adaptive time stepping, capable of high precision calculations even with velocity-dependent forces. The algorithm finds an approximate solution for the equation

$$\ddot{x} = F[\dot{x}, x, t] \tag{3.33}$$

where $\ddot{x}$ is the acceleration of the particle, and F is the force experienced by the particle dependent on velocity $\dot{x}$, position x, and time t, by expanding the equation into a truncated series of t,

$$\ddot{x}[t] \approx \ddot{x}_0 + a_0 t + a_1 t^2 + \cdots + a_6 t^7. \tag{3.34}$$

This can be re-written in terms of the time spacing $h \equiv t/dt$ and $b_k = a_k dt^{k+1}$, where dt is the step size:

$$\ddot{x}[h] \approx \ddot{x}_0 + b_0 h + b_1 h^2 + \cdots + b_6 h^7. \tag{3.35}$$

To solve for velocity and position at an arbitrary time during and at the end of the time step, we integrate the above equation once and twice respectively:

$$\dot{x}[h] \approx \dot{x}_0 + hdt \left(\ddot{x}_0 + \frac{h}{2} \left(b_0 + \frac{2h}{3} \left(b_1 + \cdots \right) \right) \right) \tag{3.36}$$

$$x[h] \approx x_0 + \dot{x}_0 hdt + \frac{h^2 dt^2}{2} \left(\ddot{x}_0 + \frac{h}{2} \left(b_0 + \frac{2h}{3} \left(b_1 + \cdots \right) \right) \right) \tag{3.37}$$

Rein & Spiegel (2014) ensure machine precision accuracy of this approximation by implementing and improving the Gauß-Radau algorithm, a 15th-order Runge-Kutta integrator pioneered by Everhart (1985). This algorithm uses an initial time spacing of $h = 0$ (at which position and velocity is already known) to determine $\ddot{x}_0$ and the coefficients a_k, b_k, later approximating the integral of $\ddot{x}[h]$ with Gauß-quadratures. Each iteration informs a recalculation of the coefficients in the expansion of $\ddot{x}[t]$ and $\ddot{x}[h]$, thereby increasing their accuracy. A 15th-order scheme is constructed through the use of a quadrature with 8 function evaluations. Step size is automatically controlled by a dimensionless parameter $\epsilon \ll 1$, chosen such that the function $x[t]$ is smooth within one time step (see Rein & Spiegel, 2014, for continued detailed explanation).

CHAPTER 4

RESULTS

4.1 Measured Gravitational Effect on Sgr A*

The results for the evolving position and velocity of Sgr A* shared various characteristics across the simulated density profiles, arguably reflecting the inherent stochastic nature of the problem at hand. Each density profile possessed a normalized distribution of velocity magnitude and total angular displacement relative to initial position of Sgr A* well-fit to a gamma distribution. Such a distribution should naturally arise as a consequence of the principle of maximum entropy (Jaynes, 1957a,b), which states that the probability distribution best representing present knowledge necessarily has the largest entropy; this minimizes the amount of prior information initially built in. The gamma distribution is appropriately the maximum entropy probability distribution for fixed, positive random variables.

In particular, the distribution of velocity magnitudes for each simulation was fit to a Maxwell-Boltzmann distribution:

$$f_{\mathbf{v}}(\mathbf{v}) = \left(\frac{3}{2\pi\sigma^2}\right)^{3/2} \exp\left[-\frac{3v^2}{2\sigma^2}\right] \tag{4.1}$$

where v is the particle velocity and σ is the velocity dispersion. The Maxwell-Boltzmann generally serves to describe the velocity distribution of a particle within a stationary environment assumed to be in equilibrium, where particle interactions only occur via brief collisions in which particles transfer energy and momentum.

In the following paragraphs and figures, I describe the relative angular deviation of Sgr A* measured at simulation times t = 1 yr, 5 yr, 10 yr, and 15 yr, along with the velocity magnitude and perpendicular velocity component magnitude.

To compute this perpendicular component, I assume it is equal to the additional orthogonal velocity components leading to $v = \sqrt{3v_\perp^2}$ or $v_\perp = \sqrt{(1/3)v^2}$. The result summaries are further supplemented by Tables 6.2 and 6.3, which list the mean and standard deviation of the distributed values. In converting distance to subtended angle, I assume a distance from the galactic center of $R_0 = 8.0$ kpc.

On average, 31922 stars were drawn in the Hernquist density profile simulation, only considering stars up to a maximum radius of 0.1 pc. The distribution of the angular shift of Sgr A* relative to its initial position after a time period of 15 years was best fit by a gamma distribution with mean 22.7 ± 5.0 μas. The distribution of velocity magnitudes for Sgr A* due to the presence of this profile was fit by a Maxwell-Boltzmann with mean 0.06 ± 0.02 km s^{-1}, with a perpendicular component magnitude of 0.04 ± 0.01 km s^{-1}.

An average of 11462 10 $M_\odot$ black holes and 358 100 $M_\odot$ black holes were drawn within the inner parsec, displacing Sgr A* on average by 20.6 ± 8.5 μas and 35.5 ± 14.9 μas respectively after 15 years. The velocity magnitude of Sgr A* induced by the 10 $M_\odot$ black holes was on average 0.05 ± 0.02 km s^{-1}, with perpendicular component of 0.03 ± 0.01 km s^{-1}. For the 100 $M_\odot$ black hole density profile, Sgr A* possessed a mean velocity magnitude of 0.09 ± 0.04 km s^{-1}, and a perpendicular component magnitude of 0.05 ± 0.02 km s^{-1}.

There was on average 4 IMBHs of mass 10^3 $M_\odot$ drawn according to our fiducial density profile within one parsec, inducing angular shifts of 39.6 ± 25.7 μas on the position of Sgr A* after 15 years. The average velocity of the central black hole induced by this profile was 0.1 ± 0.06 km s^{-1}, though unlike with other density profiles the distribution of this velocity was better fit to a general gamma distribution with mean and standard deviation 0.06 ± 0.04 km s^{-1}. The mean perpendicular

velocity component was 0.06 ± 0.04 km s^{-1}.

From the Mastrobuono-Battisti et al. density profile, an average of 10 10^4 $M_\odot$ IMBHs were drawn in the inner parsec. After 15 years, they induced an angular shift in Sgr A* position of 953.9 ± 459.0 μas, with velocity magnitude and perpendicular component of 2.63 ± 1.33 km s^{-1} and 1.57 ± 0.86 km s^{-1} respectively.

4.2 Effects on Orbital Parameters of S2

I refer you to Tables 6.4 and 6.5 for a thorough summary of the average changes in semi-major axis ($\Delta a/a$, where $a = 4.823$ mpc), eccentricity (Δe), inclination (Δi), longitude of ascending node ($\Delta\Omega$), shift of periapse ($\Delta\Theta_p$), and shift of apoapse ($\Delta\Theta_a$) induced by the stellar control and the tested discrete and smooth stellar/intermediate mass black hole density profiles. For all elements, the mean change did not scale directly with mass; 10^4 $M_\odot$ IMBHs produced the maximal average change in an orbital element, with the stellar control and 10 $M_\odot$ stellar black holes producing the next largest average changes, and the 1000 $M_\odot$ IMBHs followed by the 100 $M_\odot$ stellar black holes producing the least. Discretely realized profiles induced various mean changes in semi-major axis, differing by approximately a factor of ten ($\Delta a/a \sim 10^{-5} - 10^{-4}$) and possessing no dramatic differences from changes in semi-major axis induced by a smoothly distributed profile. Stars and low-mass stellar black holes induced changes on eccentricity with a mean of $\sim 10^{-5}$, while for 100 $M_\odot$ and 1000 $M_\odot$ black holes this value was $\sim 6 \times 10^{-6}$. The mean change in eccentricity due to 10^4 $M_\odot$ black holes was almost a factor of 100 greater at 3.76×10^{-4}. The changes in eccentricity induced by discretely distributed particles was less in all cases than those induced by the corresponding

smooth simulated profile, though by zero to two orders of magnitude.

In the second row panels of Figure 4.6, we see that smooth profiles had absolutely negligible effects on inclination and longitude of ascending node (all changing these elements by $\sim 10^{-13}$ degrees) in contrast to their discrete counterparts. Discretely distributed 10^4 $M_\odot$ IMBHs induced the largest average change of $\Delta i = 0.0539°$ and $\Delta\Omega = 0.152°$. 1000 $M_\odot$ and stellar black holes of masses 10 $M_\odot$ and 100 $M_\odot$ induced average changes of $\Delta i \approx 0.001°$ and $\Delta\Omega \approx 0.003°$, and the stellar control induced changes in i and Ω of $\sim 0.003°$ and $\sim 0.016°$ respectively.

Discretely distributed profiles also generated larger shifts in periapse and apoapse when compared to smooth distributions. For all but the 10^4 $M_\odot$ IMBH profile the mean angular shift of periapse position was $\Delta\Theta_p \lesssim 8$ μas. Shifts in apoapse position $\Delta\Theta_a$ were greater for each profile than $\Delta\Theta_p$, reaching a maximum mean of 0.97 mas with the 10^4 $M_\odot$ IMBHs. All profiles induced a mean $\Delta\Theta_a$ that was above a 10 μas threshold, reaching a next-largest value of 130 μas with the stellar control, 27.6 μas with 10 $M_\odot$ black holes, 19.8 μas with 1000 $M_\odot$ black holes, and 13.7 μas with 100 $M_\odot$ black holes.

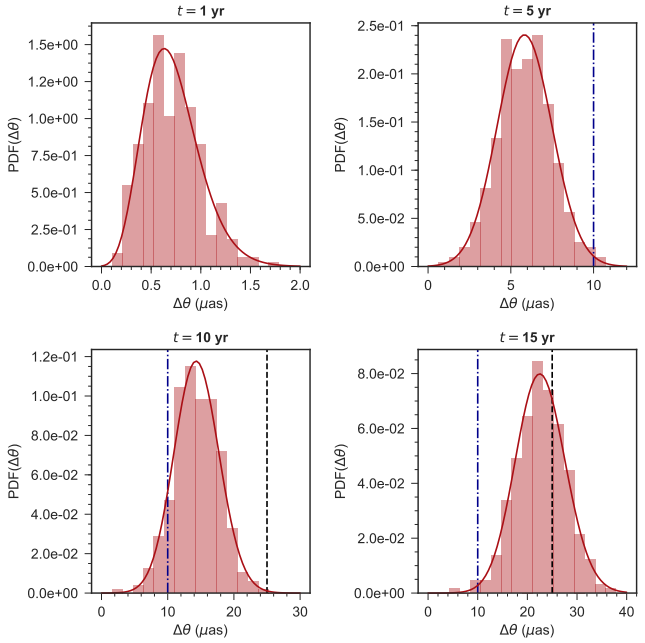

(a) Histogram representation of angular displacement of Sgr A*, induced by stellar control, as measured at four times ($\Delta t = 1$ yr, 5 yr, 10 yr, and 15 yr). Blue dot-dashed lines and black dashed line in Panel 4.1a indicate the potential maximum precision of GRAVITY (10 μas) and the EHT (25 μas) respectively.

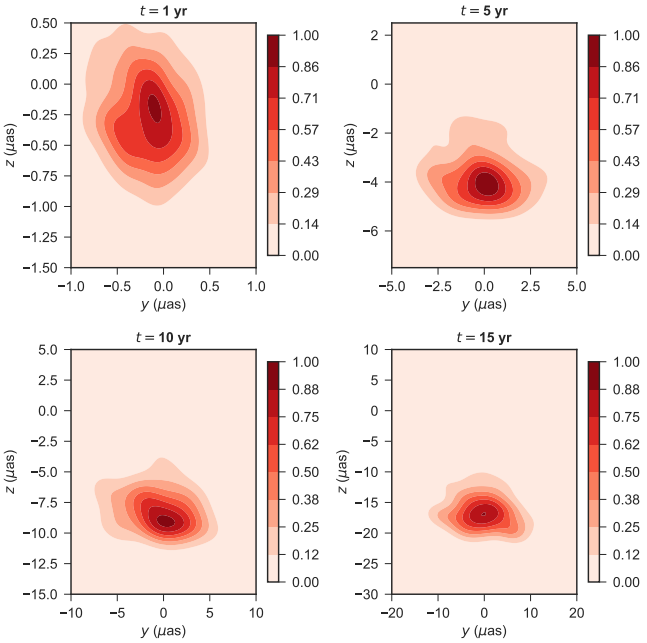

(b) Bivariate kernel density estimation of angular displacement of Sgr A*, induced by stellar control, as measured at four times ($t = 1$ yr, 5 yr, 10 yr, and 15 yr).

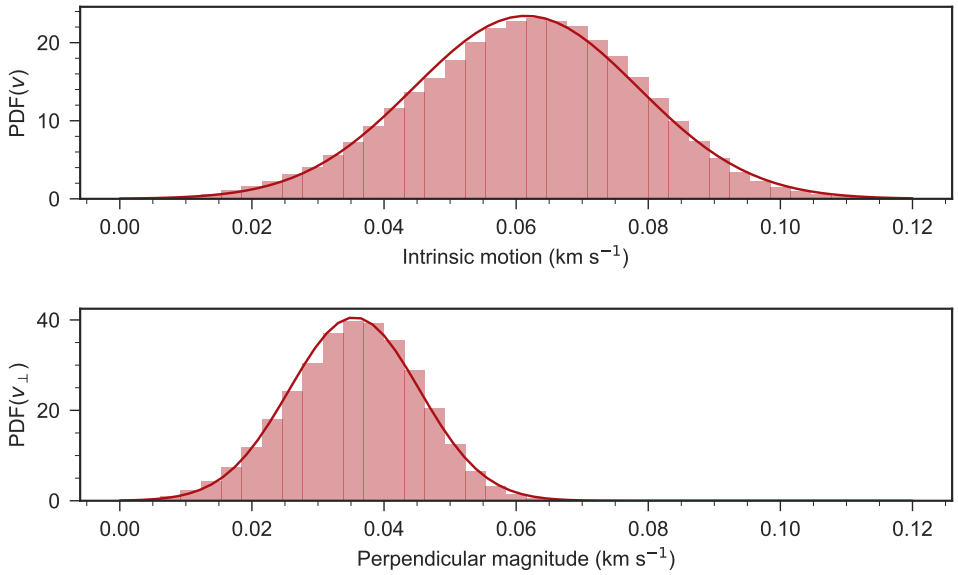

(c) Histogram distribution of intrinsic velocity magnitude and perpendicular component of the velocity of Sgr A*, induced by stellar control

Figure 4.1: The angular shift and induced velocity of Sgr A* when surrounded by stars of mass 1 $M_\odot$, distributed via a Hernquist density profile (Equation (3.1)) extending to the inner 0.1 pc.

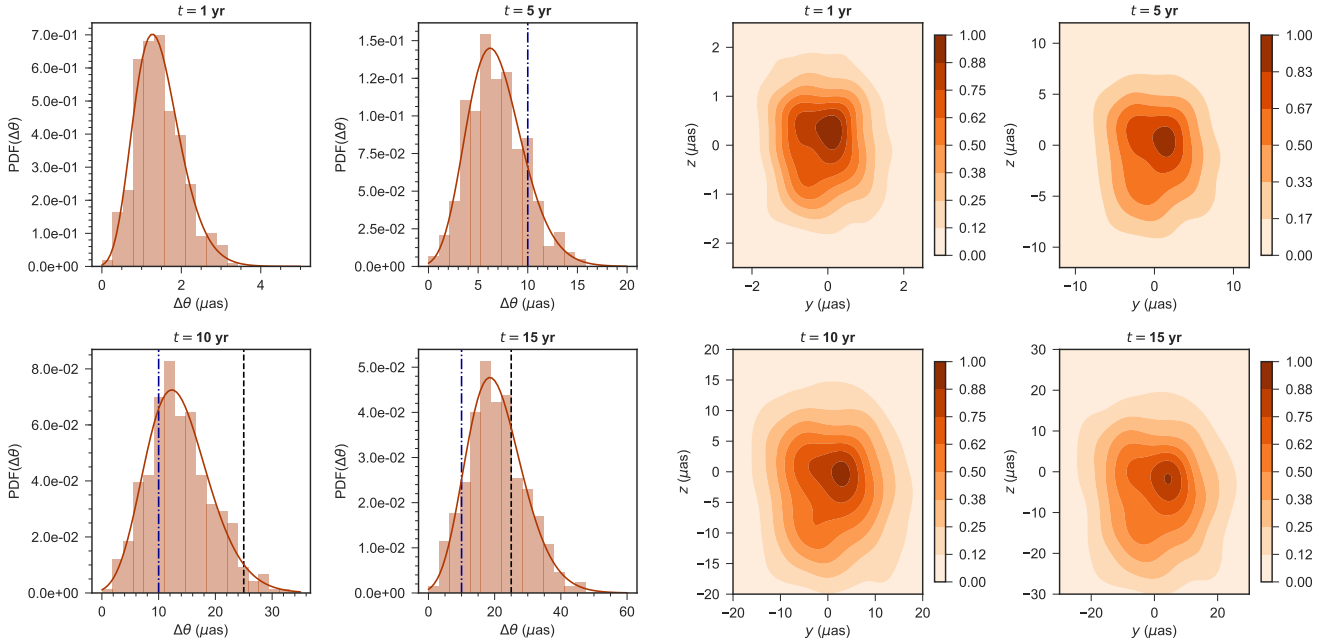

(a) Histogram representation of angular displacement of Sgr A*, induced by 10 $M_\odot$ stellar black holes.

(b) Bivariate kernel density estimation of angular displacement of Sgr A*, induced by 10 $M_\odot$ stellar black holes.

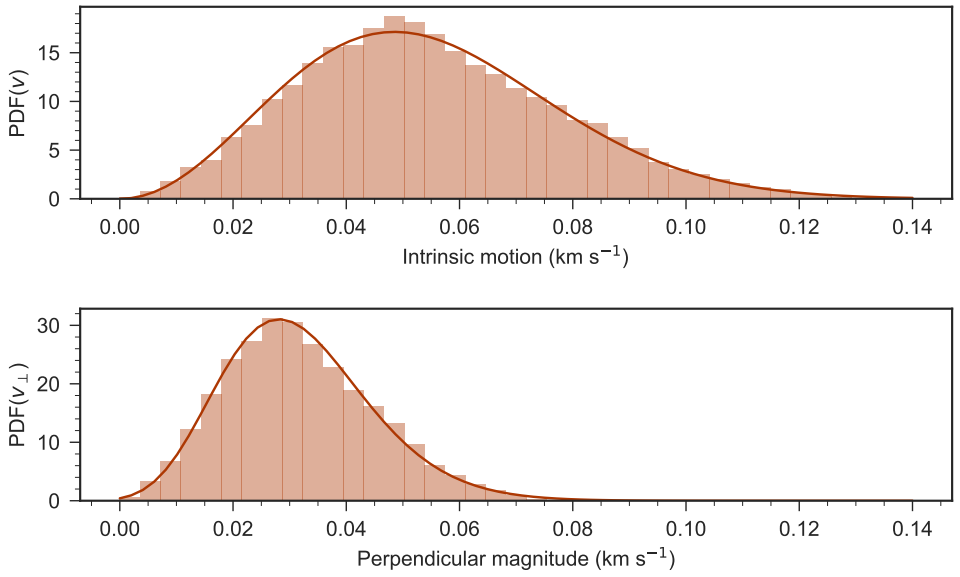

(c) Histogram distribution of intrinsic velocity magnitude and perpendicular component of the velocity of Sgr A*, induced by 10 $M_\odot$ stellar black holes.

Figure 4.2: As in Figure 4.1, with Sgr A* only surrounded by stellar black holes distributed according to the density profile of Equation (3.1.2) with $M_{\rm BH} = 10\ M_\odot$ to a maximum radius of 1 pc.

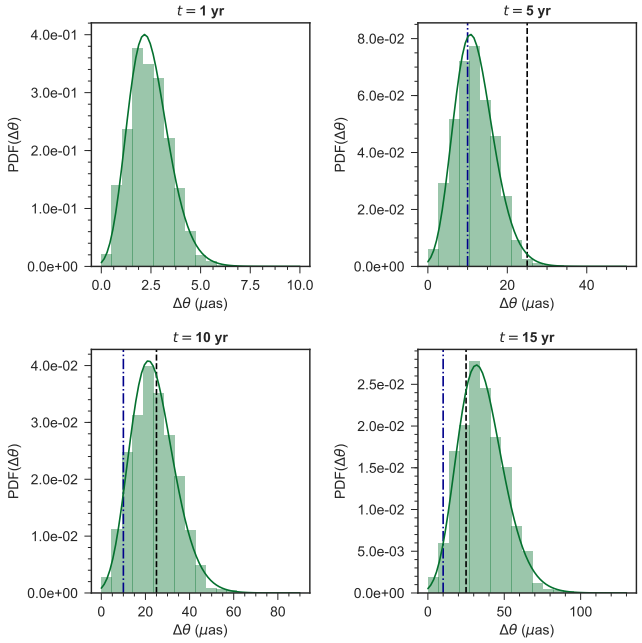

(a) Histogram representation of angular displacement of Sgr A*, induced by 100 $M_\odot$ stellar black holes.

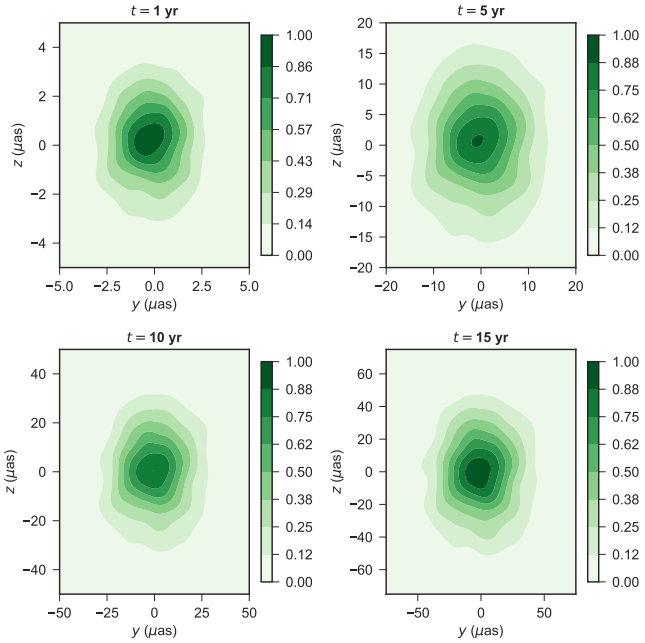

(b) Bivariate kernel density estimation of angular displacement of Sgr A*, induced by 100 $M_\odot$ stellar black holes.

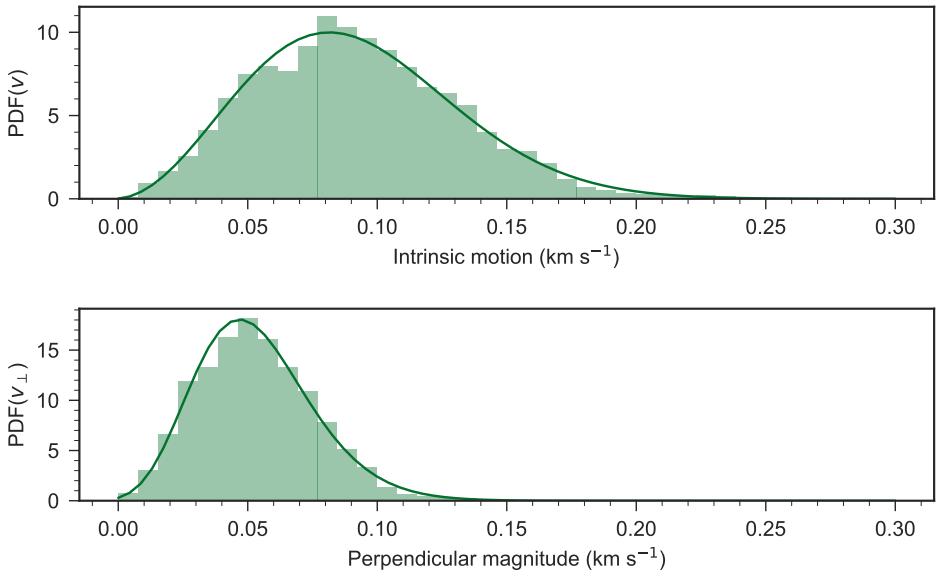

(c) Histogram distribution of intrinsic velocity magnitude and perpendicular component of the velocity of Sgr A*, induced by 100 $M_\odot$ stellar black holes.

Figure 4.3: As in 4.1, with Sgr A* only surrounded by stellar black holes distributed according to the density profile of Equation (3.1.2) with $M_{\rm BH} = 100\ M_\odot$ to a maximum radius of 1 pc.

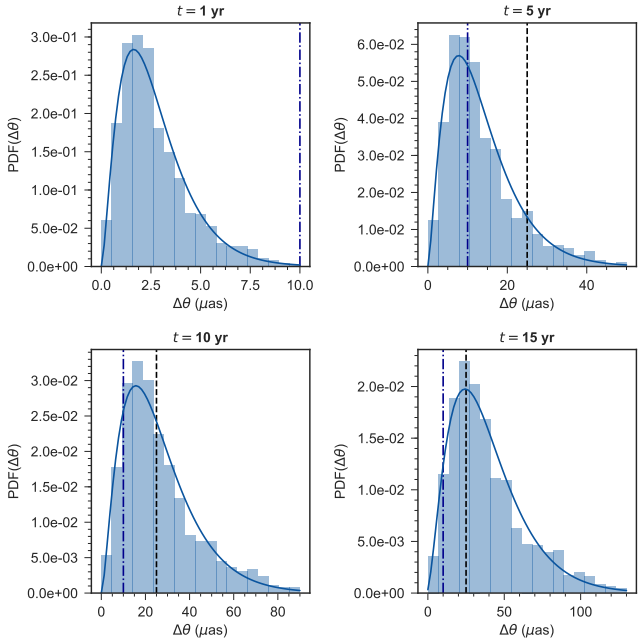

(a) Histogram representation of angular displacement of Sgr A*, induced by 1000 $M_\odot$ intermediate mass black holes.

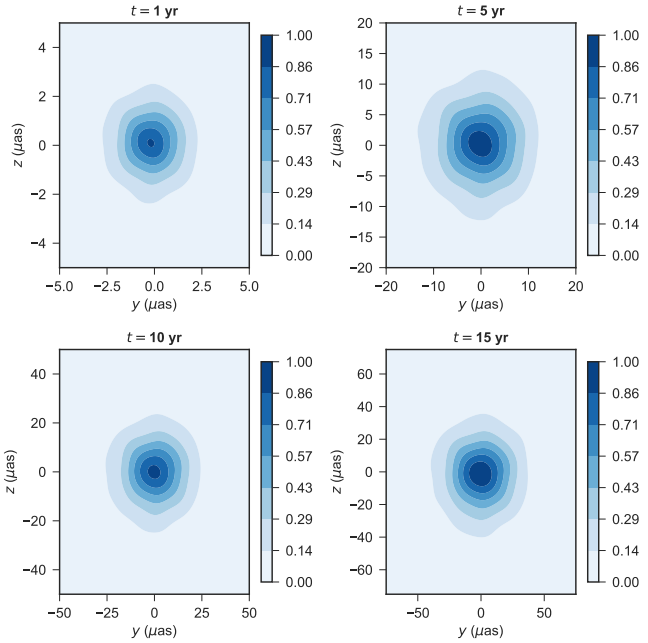

(b) Bivariate kernel density estimation of angular displacement of Sgr A*, induced by 1000 $M_\odot$ intermediate mass black holes.

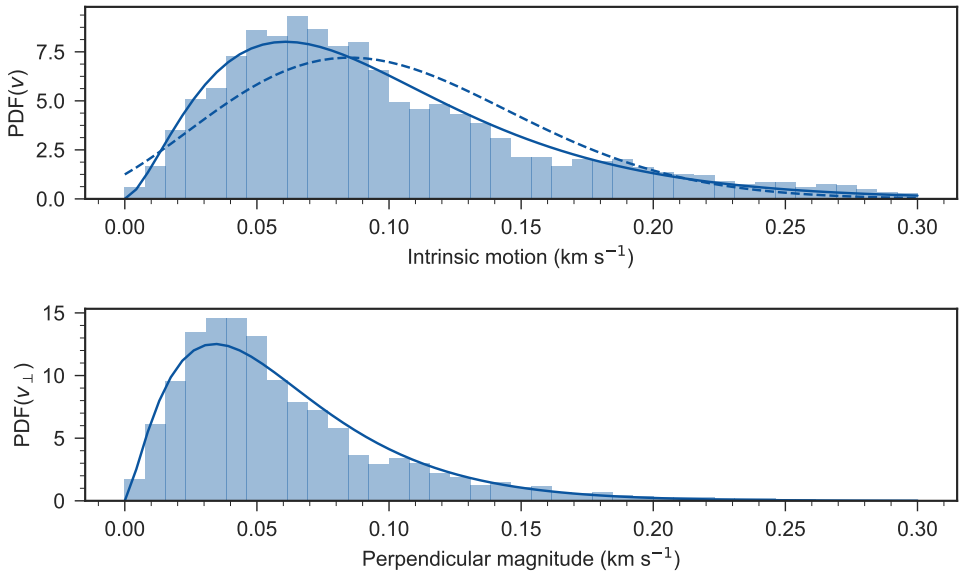

(c) Histogram distribution of intrinsic velocity magnitude and perpendicular component of the velocity of Sgr A*, induced by 1000 $M_\odot$ intermediate mass black holes. The dotted line in the upper most histogram indicates the fitted Maxwell-Boltzmann, with a mean and standard deviation of the dataset.

Figure 4.4: As in 4.1, with Sgr A* only surrounded by 1000 $M_\odot$ intermediate-mass black holes distributed according to the density profile of Equation (3.1.3) to a maximum radius of 1 pc.

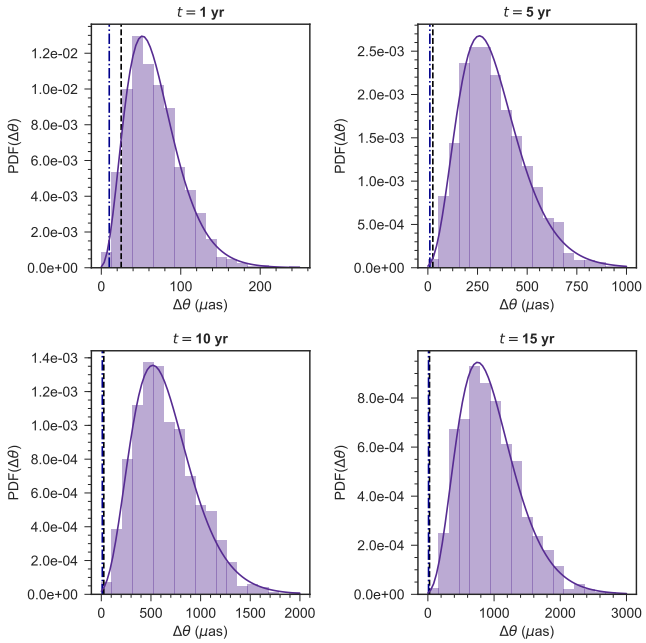

(a) Histogram representation of angular displacement of Sgr A*, induced by 10^4 $M_\odot$ intermediate mass black holes to a maximum radius of 1 pc.

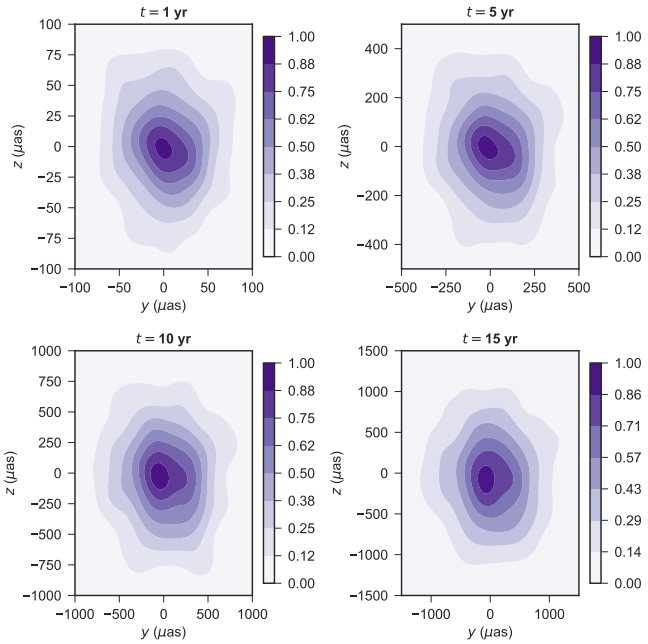

(b) Bivariate kernel density estimation of angular displacement of Sgr A*, induced by 10^4 $M_\odot$ intermediate mass black holes.

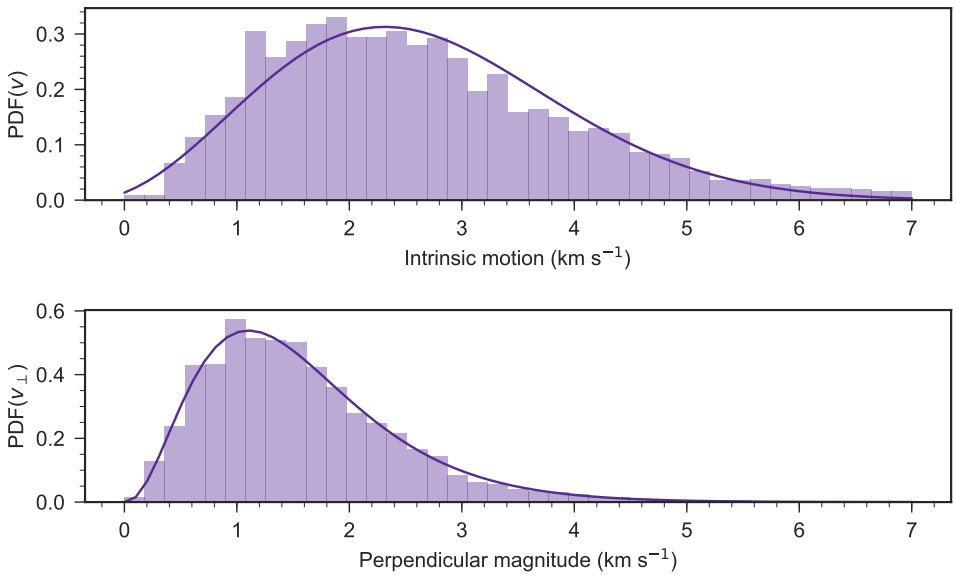

(c) Histogram distribution of intrinsic velocity magnitude and perpendicular component of the velocity of Sgr A*, induced by 10^4 $M_\odot$ intermediate mass black holes.

Figure 4.5: As in 4.1, with Sgr A* only surrounded by 10^4 $M_\odot$ intermediate-mass black holes distributed according to the density profile of Equation (3.1.3) to a maximum radius of 1 pc.

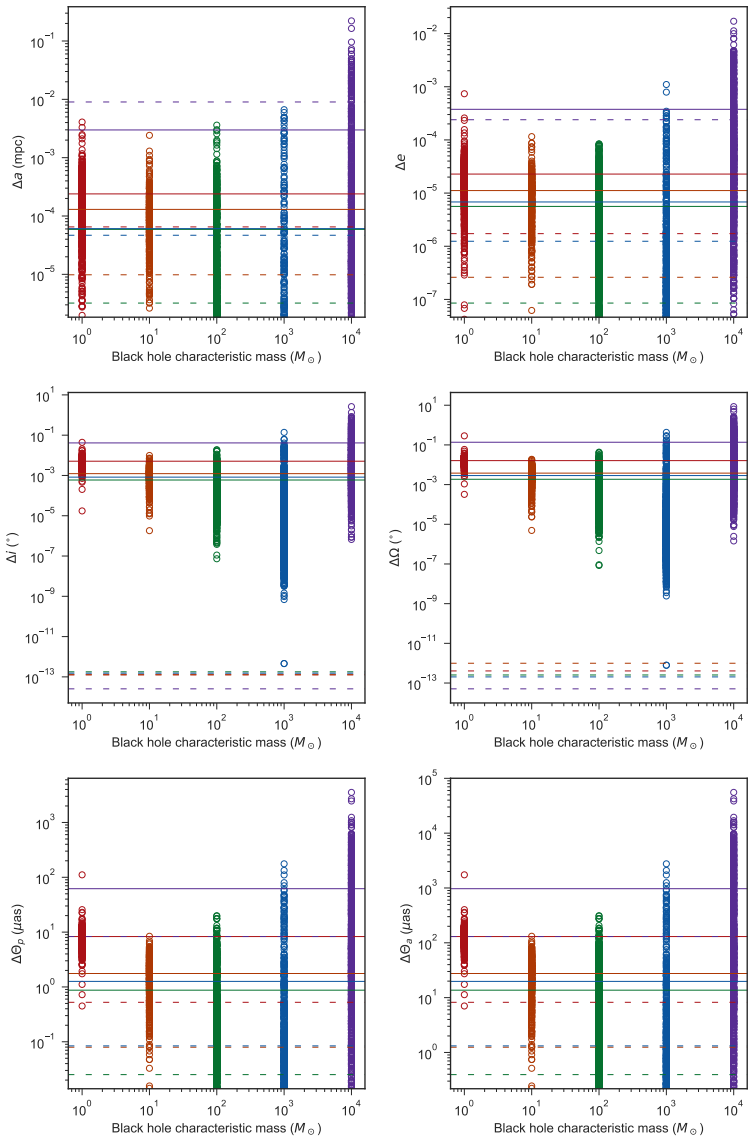

Figure 4.6: Changes in orbital elements (semi-major axis, eccentricity, inclination, longitude of ascending node, shift of periapse, and shift of apoapse) experienced by S2 during each simulation run when surrounded by tested density profiles. Red-colored data corresponds to simulations of the stellar control (Equation (3.1)), orange to 10 $M_\odot$ stellar black holes (Equation (3.1.2) with $M_{\rm BH} = 10\ M_\odot$), green to 100 $M_\odot$ stellar black holes (Equation (3.1.2) with $M_{\rm BH} = 100\ M_\odot$), blue to 1000 $M_\odot$ IMBHs (Equation (3.1.3)), and purple to 10^4 $M_\odot$ IMBHs (Equation (3.1.3).) Solid lines indicate the average change of the orbital element induced by a certain density profile, coordinated by color. Dashed lines indicate the average change of the orbital element induced by a smooth version of a certain density profile, also coordinated by color. A single circle indicates the change in orbital element that occurred in one particular simulation of S2 embedded in a certain density profile.

CHAPTER 5

DISCUSSION

Though the N-body simulations carried out in this work were based on significantly simplified assumptions, their results provide non-trivial insight into what black hole populations may or may not be both possible and detectable in the Galactic Center. Below I compare obtained results to our strongest current observational constraints, which rely on the proper motion of Sgr A* possessing a 2σ upper limit of 1.8 km s^{-1} for the velocity perpendicular to the galactic plane (Reid & Brunthaler, 2004), and the constrained error of Gillessen et al. (2009) orbital fit for S2.

With the constraint of proper motion in mind, all stellar mass and intermediate mass black hole profiles are plausible within 1 parsec. The combined precision of EHT stations ($\gtrsim$ 25 μas) would allow detection within 15 years of the angular displacement induced on Sgr A* by any of the examined profiles. The velocity induced on Sgr A* by stars and stellar black holes ($\sim$ 0.06 km s^{-1}) stand in agreement with an amplitude of Brownian motion calculated by Merritt et al. (2007); Chatterjee et al. (2002); Loeb & Furlanetto (2013), using $\langle m_* \rangle = 1\ M_\odot$ and $M_{\rm BH} = 4.4 \times 10^6\ M_\odot$ (See Equation (1.18)), as well as N-body simulations of stars within the inner 2 pc performed by Reid & Brunthaler (2004). Both 100 $M_\odot$ and 1000 $M_\odot$ black holes induced angular shifts in the position of Sgr A* at a rate of $\gtrsim 2\ \mu$as yr^{-1}. The mean velocity of Sgr A* when surrounded by each profile is on the order of 0.1 km s^{-1}, closer to estimates on velocity out of the disk as outlined by Reid & Brunthaler (2004) than results from other profiles. However, due to their similar dynamical signature the tested profiles for 100 $M_\odot$ and 1000 $M_\odot$ black holes are arguably impossible to differentiate from their gravitational effect on Sgr

A* alone. The 10^4 $M_\odot$ IMBH profile produced the largest angular shifts, with a mean of $\sim$ 65 μas yr^{-1}. It additionally induced the largest intrinsic velocity of 2.62 ± 1.35 km s^{-1}. The perpendicular component of this was 1.6 ± 0.9 km s^{-1}, the mean of which is just within the present 2σ limit of 1.8 km s^{-1} (Reid & Brunthaler, 2004).

To properly examine the impact of these density profiles on S2, let us first review the current accuracies in VLT and Keck data embedded in errors allotted for by Gillessen et al. (2009). The best fitted values for semi-major axis and eccentricity are accurate to ~ 2 mas and 3×10^{-3} respectively, and the inclination, longitude of ascending note, and argument of periapse are accurate to $0.72° - 0.81°$. To properly use the orbit of S2 as a probe for stellar remnants and intermediate mass black holes, the changes induced by these dark objects must necessarily fit within these accuracies while additionally surpassing orbital changes associated with relativistic effects. Grould et al. (2017) have investigated the potential of GRAVITY to detect various relativistic effects on the S2, concluding that a shift of periapse due to relativistic advance will be 30 μas in 14 years (roughly 34 μas per revolution.) Alternatively Gualandris et al. (2010) calculate the displacement in the star's apoapse as

$$\Delta r_a \approx a(1+e)\Delta\varpi \approx \frac{6\pi G M_{\rm Sgr}}{c^2(1-e)} \tag{5.1}$$

where $\Delta\varpi = \Delta(\Omega+\omega)$ is the advance in periapse angle. Using $M_{\rm Sgr} = 4.4 \times 10^6$ $M_\odot$ and $R_0 = 8$ kpc, Δr_a subtends an angle on the sky $\Delta\Theta_a = 0.86$ mas. The angle on the sky subtended by the displacement in the star's periapse can then be calculated as $\Delta\Theta_p = \Delta\Theta_a(1-e)/(1+e) \approx 54.9$ μas. Thus in $\Delta\Theta_a$ and $\Delta\Theta_p$, along with constrained errors of a, e, i, Ω, and ω, we have lower limits and upper limits respectively to determine the detectability of a certain density profile's dynamical signature on S2.

There is a notable difference of the dynamical effect of smooth and discrete distributions in orbital arguments pertaining to angle (i and Ω). A smooth or centralized distribution creates virtually no changes in these parameters, whereas the gravitational effect of discretely distributed particles generates distinct apsidal precession of the orbit of S2. The average change in i and Ω for all density profiles are within current error of 0.7°. It is interesting to note that the mean change in inclination and longitude of ascending node due to the stellar control and 10 $M_\odot$ stellar mass black holes exceeds that induced by 100 $M_\odot$ stellar black holes and 1000 $M_\odot$ IMBHs. This may be because, due to their increased number density, these smaller objects experience closer encounters with S2 that more intensely perturb its orbit. However, stars, stellar black holes, and 1000 $M_\odot$ IMBHs all induced changes in periapse and apoapse under estimated relativistic shifts, implying that these density profiles are not detectable through observation of S2's orbital precession. Only the 10^4 $M_\odot$ IMBH profile induced changes in these parameters exceeding the lower limit placed by the relativistic effects. With this, S2 appears to be a more effective probe for detecting intermediate mass black holes of mass $\gtrsim 10^4$ $M_\odot$. Particularly through observations of $\sim$ milli-arcsecond angular shifts in apoapse, along with perceptible changes in inclination and longitude of ascending node, we can infer the existence of surrounding discrete objects.

This work can be improved upon in a number of ways, primarily in an inclusion of a larger variety of density profiles and improved numerical methods. I chose to test a few profiles that literature has provided, as they reflect conclusions of significant theoretical work. However, the total cluster mass of both stellar and intermediate mass black holes of the varying characteristic masses remain an independent variable. The results gathered here may be expanded upon through examination of high-abundance and low-abundance cases of the tested density pro-

files, to further refine limits on black hole density profiles given current astrometric constraints. In a similar vein, more information may be obtained through examining spherically asymmetric profiles. For both Sgr A* and S2, the experienced gravitational effect depends both on the characteristic and cumulative mass, as well as spherical symmetry of a surrounding density profile. While an object embedded within a spherically symmetric mass comprised of numerous but discrete particles experiences an induced Brownian motion proportional to typical particle mass, an asymmetric distribution of particles generates a larger amplitude wobble reflecting the skewed distribution. This may have already played a role in simulations of the 10^4 $M_\odot$ IMBH profile, where the assumed spherical symmetry was compromised by a relatively small number density and larger gravitational effects on Sgr A* and S2 were generated.

Even though this work identified a potentially observable IMBH black hole density profile through its gravitational effects on S2, this effect may be replicable by alternative unseen matter or a single large IMBH. Thus it is critical to understand how the magnitude of these changes evolve over multiple periods of S2's orbit, and whether such information is in fact indicative of the total mass and concentration of the gravitationally influencing objects. In general, future N-body simulations on this subject would do well to consider how the combined gravitational effects of these objects might manifest in the Galactic Center. An ideal simulation would be a relaxed orbital system populated with stars, stellar black holes, and intermediate-mass black holes in the inner parsec. How their combined dynamical effect reveals itself will be contingent on the particular number and distribution of each object. This may be better investigated with higher-order integration schemes that satisfactory incorporate direct integration and symplectic methods, treating all particles in the system as gravitationally active.

CHAPTER 6

DATA TABLES

	$\langle m_\rho \rangle = 1\ M_\odot$	$\langle m_\rho \rangle = 10\ M_\odot$	$\langle m_\rho \rangle = 100\ M_\odot$	$\langle m_\rho \rangle = 10^3\ M_\odot$	$\langle m_\rho \rangle = 10^4\ M_\odot$
Error threshold					
Discrete	1×10^{-4}	1×10^{-7}	10^{-7}	10^{-7}	10^{-7}
Smooth	10^{-4}	10^{-5}	10^{-5}	10^{-4}	5×10^{-3}
N_{runs} successful	309	413	1299	1394	943
$N_{\text{particles}}$					
Mean	31922	11462	358	4	10
Max	32069 [0.3%]	11623 [0.2%]	405 [0.1%]	5 [17.8%]	14 [1.5%]
Min	31770 [0.3%]	11272 [0.2%]	321 [0.1%]	0 [0.1%]	5 [0.5%]

Table 6.1: The error threshold determining which simulations of discrete and smooth density profiles were analyzed, number of successful simulation runs (out of 1500), and the average, minimum, and maximum number of particles drawn from the tested density profiles. Bracketed percentages indicate the percentage of runs that involved the maximum or minimum number of particles.

	$\langle m_\rho \rangle = 1\ M_\odot$		$\langle m_\rho \rangle = 10\ M_\odot$		$\langle m_\rho \rangle = 100\ M_\odot$		$\langle m_\rho \rangle = 10^3\ M_\odot$		$\langle m_\rho \rangle = 10^4\ M_\odot$	
	μ	σ	μ	σ	μ	σ	μ	σ	μ	σ
$\Delta\theta$ (μas)										
1 yr	0.7	0.3	1.2	0.6	2.4	1	2.8	1.9	67.8	33.8
5 yr	5.8	1.66	6.9	2.8	11.9	5	13.6	9.2	333.8	165.8
10 yr	14.4	3.4	12.7	5.6	23.6	10	26.8	17.8	654.9	321.2
15 yr	22.7	5	20.6	8.5	35.5	14.9	39.6	25.7	953.9	459

Table 6.2: Mean (μ) and standard deviation (σ) of the angular displacement of Sgr A*, measured relative to its original position, induced by discrete density profiles describing the distribution of stars ($\langle m_\rho \rangle = 1\ M_\odot$), stellar black holes ($\langle m_\rho \rangle = 10\ M_\odot,\ 100\ M_\odot$), and intermediate mass black holes ($\langle m_\rho \rangle = 1000\ M_\odot,\ 10^4\ M_\odot$). See Figures 4.1 to 4.5 for its visual representation.

	$\langle m_\rho \rangle = 1\ M_\odot$		$\langle m_\rho \rangle = 10\ M_\odot$		$\langle m_\rho \rangle = 100\ M_\odot$		$\langle m_\rho \rangle = 10^3\ M_\odot$		$\langle m_\rho \rangle = 10^4\ M_\odot$	
	μ	σ	μ	σ	μ	σ	μ	σ	μ	σ
$\lvert v \rvert$ (km s^{-1})	0.06	0.02	0.05	0.02	0.09	0.04	0.1	0.06	2.63	1.33
$\lvert v_\perp \rvert$ (km s^{-1})	0.04	0.01	0.03	0.01	0.05	0.02	0.06	0.04	1.57	0.86

Table 6.3: Mean (μ) and standard deviation (σ) of the absolute intrinsic velocity and its perpendicular component of Sgr A*, induced by discrete density profiles describing the distribution of stars ($\langle m_\rho \rangle = 1\ M_\odot$), stellar black holes ($\langle m_\rho \rangle = 10\ M_\odot,\ 100\ M_\odot$), and intermediate mass black holes ($\langle m_\rho \rangle = 1000\ M_\odot,\ 10^4\ M_\odot$). The table is visualized in Figures 4.1 to 4.5.

	$\langle m_\rho \rangle = 1\ M_\odot$	$\langle m_\rho \rangle = 10\ M_\odot$	$\langle m_\rho \rangle = 100\ M_\odot$	$\langle m_\rho \rangle = 10^3\ M_\odot$	$\langle m_\rho \rangle = 10^4\ M_\odot$
$\underline{\Delta a/a}$					
Mean					
Discrete	4.14E-05	2.07E-05	1.22E-05	1.26E-05	6.21E-04
Smooth	1.35E-05	2.03E-06	6.63E-07	9.67E-06	1.86E-03
$\underline{\Delta e}$					
Mean					
Discrete	2.28E-05	1.12E-05	5.61E-06	6.81E-06	3.76E-04
Smooth	1.73E-06	2.61E-07	8.53E-08	1.24E-06	2.40E-04

Table 6.4: Average changes induced by discrete and smooth density profiles describing the distribution of stars ($\langle m_\rho \rangle = 1\ M_\odot$), stellar black holes ($\langle m_\rho \rangle = 10\ M_\odot,\ 100\ M_\odot$), and intermediate mass black holes ($\langle m_\rho \rangle = 1000\ M_\odot,\ 10^4\ M_\odot$) on the semi-major axis ($\Delta a/a$, with $a \sim 5$ mpc) and eccentricity (e) of S2.

	$\langle m_\rho \rangle = 1\ M_\odot$	$\langle m_\rho \rangle = 10\ M_\odot$	$\langle m_\rho \rangle = 100\ M_\odot$	$\langle m_\rho \rangle = 10^3\ M_\odot$	$\langle m_\rho \rangle = 10^4\ M_\odot$
Δi (deg)					
Mean					
Discrete	5.10E-03	1.23E-03	5.94E-04	8.25E-04	4.13E-02
Smooth	1.27E-13	1.27E-13	1.78E-13	1.53E-13	2.54E-14
$\Delta\Omega$ (deg)					
Mean					
Discrete	1.62E-02	3.79E-03	1.86E-03	2.85E-03	1.36E-01
Smooth	4.07E-13	9.92E-13	2.54E-13	2.04E-13	5.09E-14
$\Delta\Theta_p$ (μas)					
Mean					
Discrete	8.3	1.8	0.9	1.3	61.9
Smooth	0.5	0.08	0.03	0.08	8.3
$\Delta\Theta_a$ (μas)					
Mean					
Discrete	130	27.6	13.7	19.8	970.4
Smooth	8.2	1.3	0.4	1.3	130.2

Table 6.5: Average changes induced by discrete and smooth density profiles describing the distribution of stars ($\langle m_\rho \rangle = 1\ M_\odot$), stellar black holes ($\langle m_\rho \rangle = 10\ M_\odot,\ 100\ M_\odot$), and intermediate mass black holes ($\langle m_\rho \rangle = 1000\ M_\odot,\ 10^4\ M_\odot$) on the inclination, longitude of the periapsis, angular shift of periapse, and angular shift of apoapse (i, Ω, $\Delta\Theta_p$, and $\Delta\Theta_a$) of S2.

APPENDIX A

ENCLOSED MASS, ACCELERATION, AND GRAVITATIONAL POTENTIAL OF A GENERALIZED DENSITY CUSP

Consider a density profile describing a particle system characterized by a cusp:

$$\rho(r) = \rho_0 \left(\frac{r}{r_0}\right)^{-\gamma} \tag{A.1}$$

where $\gamma > 0$.

First, we determine enclosed mass, acceleration, and gravitational potential for the density profiles with $2 < \gamma < 3$. The enclosed mass is calculated through a surface integral of Equation (A).

$$\begin{aligned} M(<r) &= \int_0^r 4\pi s^2 \rho(s) ds \\ &= 4\pi\rho_0 \int_0^r s^2 \left(\frac{s}{r_0}\right)^{-\gamma} ds \\ &= \frac{4\pi\rho_0}{r_0^{-\gamma}} \int_0^r s^{2-\gamma} ds \\ &= \frac{4\pi\rho_0}{r_0^{-\gamma}} \frac{1}{3-\gamma} s^{3-\gamma}\Big|_{s=0}^{s=r} \\ &= \frac{4\pi r^3 \rho_0}{3-\gamma} \left(\frac{r}{r_0}\right)^{-\gamma} \end{aligned} \tag{A.2}$$

Note that $M(<r) < 0$ for $\gamma > 3$, therefore such γ values correspond to unphysical systems.

From Newton's law of gravitation, the force experienced by a particle with mass m at position $\mathbf{r}$ is $F(\mathbf{r}) = m\mathbf{a} = -GmM(<r)/r^2\ \hat{\mathbf{r}}$. This implies the acceleration

experienced by the particle is

$$\begin{aligned}
\mathbf{a}(\mathbf{r}) &= \frac{-GM(<r)}{r^2}\,\widehat{\mathbf{r}} \\
&= \frac{-4\pi G r^3 \rho_0}{(3-\gamma)r^2}\left(\frac{r}{r_0}\right)^{-\gamma}\,\widehat{\mathbf{r}} \\
&= \frac{-4\pi G r \rho_0}{(3-\gamma)}\left(\frac{r}{r_0}\right)^{-\gamma}\,\widehat{\mathbf{r}}
\end{aligned} \tag{A.3}$$

From the acceleration, we can determine the gravitational potential of the density profile:

$$\begin{aligned}
\mathbf{a}(\mathbf{r}) &= -\nabla\Phi(\mathbf{r}) = -\left.\frac{\partial\Phi}{\partial s}\right|_{s=r}\widehat{\mathbf{r}} \\
\Phi(r) &= -\int_r^\infty \mathbf{a}(\mathbf{s})\cdot d\mathbf{s} \\
&= \frac{4\pi G\rho_0}{(3-\gamma)r_0^{-\gamma}}\int_r^\infty s^{1-\gamma}ds \\
&= \frac{4\pi G\rho_0}{(3-\gamma)r_0^{-\gamma}}\frac{1}{2-\gamma}s^{2-\gamma}\Big|_{s=r}^{s=\infty} \\
&= -\frac{4\pi G r^2\rho_0}{(3-\gamma)(\gamma-2)}\left(\frac{r}{r_0}\right)^{-\gamma}
\end{aligned} \tag{A.4}$$

In the case of $\gamma = 2$ (the isothermal sphere), Equations (A.2) and (A.3) still hold. Specifically,

$$\begin{aligned}
M(<r) &= 4\pi r_0^3\rho_0\left(\frac{r}{r_0}\right) \\
\mathbf{a}(\mathbf{r}) &= -4\pi G r_0\rho_0\left(\frac{r}{r_0}\right)^{-1}
\end{aligned}$$

Given that $|\mathbf{a}| \propto r^{-1}$, gravitational potential is proportional to the natural logarithm of r:

$$\begin{aligned}
\Phi(r) &= -\int_r^\infty \mathbf{a}(\mathbf{s})\cdot d\mathbf{s} \\
&= 4\pi G r_0\rho_0\int_r^\infty\left(\frac{s}{r_0}\right)^{-1}ds \\
&= 4\pi G r_0^2\rho_0\ln\left(\frac{r}{r_0}\right)
\end{aligned}$$

though this is undefined as $r \to \infty$. Such a divergence occurs for any $\gamma < 2$, hence for a density profile $\rho \propto r^{-\gamma}$ ($\gamma < 2$) there must be an indicated truncated radius $r_{\max}$ such that for $r > r_{\max}$, $\Phi(r) = 0$.

BIBLIOGRAPHY

Abbott, B. P., Abbott, R., Abbott, T., et al. 2016, Physical review letters, 116, 061102

Abel, T., Bryan, G. L., & Norman, M. L. 2000, The Astrophysical Journal, 540, 39

Abuter, R., Accardo, M., Amorim, A., et al. 2017, arXiv preprint arXiv:1705.02345

Alexander, T., & Hopman, C. 2009, The Astrophysical Journal, 697, 1861

Allen, D. A., Hyland, A., & Hillier, D. 1990, Monthly Notices of the Royal Astronomical Society, 244, 706

Antonini, F., Capuzzo-Dolcetta, R., Mastrobuono-Battisti, A., & Merritt, D. 2012, The Astrophysical Journal, 750, 111

Bahcall, J., & Wolf, R. 1977, The Astrophysical Journal, 216, 883

Bahcall, J. N., & Wolf, R. A. 1976, The Astrophysical Journal, 209, 214

Bailyn, C. D., Jain, R. K., Coppi, P., & Orosz, J. A. 1998, The Astrophysical Journal, 499, 367

Balick, B., & Brown, R. L. 1974, The Astrophysical Journal, 194, 265

Bañados, E., Venemans, B. P., Mazzucchelli, C., et al. 2018, Nature, 553, 473

Battaglia, G., Helmi, A., Morrison, H., et al. 2005, Monthly Notices of the Royal Astronomical Society, 364, 433

Baumgardt, H., Hut, P., Makino, J., McMillan, S., & Zwart, S. P. 2002, The Astrophysical Journal Letters, 582, L21

Begelman, M. C., Blandford, R. D., & Rees, M. J. 1984, Reviews of Modern Physics, 56, 255

Belloni, T. M., Sanna, A., & Méndez, M. 2012, Monthly Notices of the Royal Astronomical Society, 426, 1701

Binney, J., & Tremaine, S. 2011, Galactic dynamics (Princeton university press)

Broderick, A. E., Loeb, A., & Reid, M. J. 2011, The Astrophysical Journal, 735, 57

Bromm, V., Coppi, P. S., & Larson, R. B. 1999, The Astrophysical Journal, 527, L5

Bromm, V., & Loeb, A. 2003, The Astrophysical Journal, 596, 34

Chambers, J. E. 1999, Monthly Notices of the Royal Astronomical Society, 304, 793

Chandrasekhar, S. 1941, The Astrophysical Journal, 94, 511

—. 1943, The Astrophysical Journal, 97, 255

Chatterjee, P., Hernquist, L., & Loeb, A. 2002, The Astrophysical Journal, 572, 371

Chirikov, B. V. 1979, Physics reports, 52, 263

Cohn, H., & Kulsrud, R. M. 1978, The Astrophysical Journal, 226, 1087

Coleman Miller, M., & Colbert, E. J. 2004, International Journal of Modern Physics D, 13, 1

Di Matteo, T., Springel, V., & Hernquist, L. 2005, Nature, 433, 604

Doeleman, S. S., Weintroub, J., Rogers, A. E., et al. 2008, Nature, 455, 78

Dragt, A., Neri, F., Rangarajan, G., et al. 1988, Annual Review of Nuclear and Particle Science, 38, 455

Dragt, A. J., & Finn, J. M. 1976, Journal of Mathematical Physics, 17, 2215

Eckart, A., & Genzel, R. 1996, Nature, 383, 415

—. 1997, Monthly Notices of the Royal Astronomical Society, 284, 576

Eisenhauer, F., Genzel, R., Alexander, T., et al. 2005, The Astrophysical Journal, 628, 246

Eisenhauer, F., Perrin, G., Brandner, W., et al. 2008, in Optical and Infrared Interferometry, Vol. 7013, International Society for Optics and Photonics, 70132A

Everhart, E. 1985, in International Astronomical Union Colloquium, Vol. 83, Cambridge University Press, 185–202

Ferrarese, L., & Merritt, D. 2000, The Astrophysical Journal, 539, L9

Figer, D. F., Najarro, F., Morris, M., et al. 1996, The Astrophysical Journal, 506, 384

Fish, V. L., Doeleman, S. S., Beaudoin, C., et al. 2011, The Astrophysical Journal Letters, 727, L36

Freitag, M., Amaro-Seoane, P., & Kalogera, V. 2006, The Astrophysical Journal, 649, 91

Freitag, M., & Benz, W. 2002, Astronomy & Astrophysics, 394, 345

Ge, Z., & Marsden, J. E. 1988, Phys. Lett. A, 133, 134

Gebhardt, K., Rich, R. M., & Ho, L. C. 2002, The Astrophysical Journal Letters, 578, L41

Gebhardt, K., Bender, R., Bower, G., et al. 2000, The Astrophysical Journal, 539, L13

Genzel, R., Eckart, A., Ott, T., & Eisenhauer, F. 1997, Monthly Notices of the Royal Astronomical Society, 291, 219

Genzel, R., Pichon, C., Eckart, A., Gerhard, O., & Ott, T. 2000, Monthly Notices of the Royal Astronomical Society, 317, 348

Genzel, R., Schödel, R., Ott, T., et al. 2003, Nature, 425, 934

Genzel, R., Thatte, N., Krabbe, A., Kroker, H., & Tacconi-Garman, L. 1996, The Astrophysical Journal, 472, 153

Gerhard, O. 2000, The Astrophysical Journal Letters, 546, L39

Ghez, A., Klein, B., Morris, M., & Becklin, E. 1998, The Astrophysical Journal, 509, 678

Ghez, A., Salim, S., Hornstein, S., et al. 2005, The Astrophysical Journal, 620, 744

Ghez, A., Duchêne, G., Matthews, K., et al. 2003, The Astrophysical Journal Letters, 586, L127

Ghez, A., Salim, S., Weinberg, N., et al. 2008, The Astrophysical Journal, 689, 1044

Giersz, M., Leigh, N., Hypki, A., Askar, A., & Lützgendorf, N. 2016, arXiv preprint arXiv:1607.08384

Gillessen, S., Eisenhauer, F., Trippe, S., et al. 2009, The Astrophysical Journal, 692, 1075

Gillessen, S., Eisenhauer, F., Perrin, G., et al. 2010, in Optical and Infrared Interferometry II, Vol. 7734, International Society for Optics and Photonics, 77340Y

Gladman, B., Duncan, M., & Candy, J. 1991, Celestial Mechanics and Dynamical Astronomy, 52, 221

Graham, A. W. 2016, in Astrophysics and Space Science Library, Vol. 418, Galactic Bulges, ed. E. Laurikainen, R. Peletier, & D. Gadotti, 263

Graham, A. W., & Driver, S. P. 2007, The Astrophysical Journal, 655, 77

Graham, A. W., Erwin, P., Caon, N., & Trujillo, I. 2001, The Astrophysical Journal Letters, 563, L11

Grould, M., Vincent, F., Paumard, T., & Perrin, G. 2017, Astronomy & Astrophysics, 608, A60

Gualandris, A., Gillessen, S., & Merritt, D. 2010, Monthly Notices of the Royal Astronomical Society, 409, 1146

Gualandris, A., & Merritt, D. 2009, The Astrophysical Journal, 705, 361

Gürkan, M. A., Freitag, M., & Rasio, F. A. 2004, The Astrophysical Journal, 604, 632

Hailey, C. J., Mori, K., Bauer, F. E., et al. 2018, Nature, 556, 70

Hairer, E., Lubich, C., & Wanner, G. 2006, Geometric numerical integration: structure-preserving algorithms for ordinary differential equations, Vol. 31 (Springer Science & Business Media)

Hansen, B. M., & Milosavljević, M. 2003, The Astrophysical Journal Letters, 593, L77

Hernquist, L. 1990, The Astrophysical Journal, 356, 359

Hosokawa, M., Jauncey, D., Reynolds, J., et al. 2002, The Astrophysical Journal Letters, 580, L43

Israel, W. 1967, Physical Review, 164, 1776

Jansky, K. G. 1933, Nature, 132, 66

Jaynes, E. T. 1957a, Physical review, 106, 620

—. 1957b, Physical review, 108, 171

Jerjen, H., Binggeli, B., & Freeman, K. 2000, The Astronomical Journal, 119, 593

Kellermann, K., & Moran, J. 2001, Annual Review of Astronomy and Astrophysics, 39, 457

Kim, S. S., Figer, D. F., & Morris, M. 2004, The Astrophysical Journal Letters, 607, L123

Kim, S. S., & Morris, M. 2003, The Astrophysical Journal, 597, 312

Kızıltan, B., Baumgardt, H., & Loeb, A. 2017, Nature, 541, 203

Kormendy, J., & Ho, L. C. 2013, ArXiv e-prints

Kozai, Y. 1962, The Astronomical Journal, 67, 591

Lacy, J., Baas, F., Townes, C., & Geballe, T. 1979, The Astrophysical Journal, 227, L17

Lacy, J. H., Townes, C. H., Geballe, T. R., & Hollenbach, D. J. 1980, The Astrophysical Journal, 241, 132

Laurikainen, E., Salo, H., Buta, R., Knapen, J., & Comerón, S. 2010, Monthly Notices of the Royal Astronomical Society, 405, 1089

Leigh, N. W., Böker, T., Maccarone, T. J., & Perets, H. B. 2013, Monthly Notices of the Royal Astronomical Society, 429, 2997

Lightman, A., & Shapiro, S. 1977, The Astrophysical Journal, 211, 244

Löckmann, U., & Baumgardt, H. 2008, Monthly Notices of the Royal Astronomical Society, 384, 323

Loeb, A., & Furlanetto, S. R. 2013, The first galaxies in the universe (Princeton University Press)

Lynden-Bell, D., & Rees, M. J. 1971, Monthly Notices of the Royal Astronomical Society, 152, 461

Madau, P., & Rees, M. J. 2001, The Astrophysical Journal Letters, 551, L27

Mastrobuono-Battisti, A., Perets, H. B., & Loeb, A. 2014, The Astrophysical Journal, 796, 40

McConnell, N. J., & Ma, C.-P. 2013, The Astrophysical Journal, 764

McConnell, N. J., Ma, C.-P., Gebhardt, K., et al. 2011, Nature, 480, 215

McMillan, S. L., & Zwart, S. F. P. 2003, The Astrophysical Journal, 596, 314

Merritt, D. 2010, The Astrophysical Journal, 718, 739

Merritt, D., Berczik, P., & Laun, F. 2007, The Astronomical Journal, 133, 553

Merritt, D., & Ferrarese, L. 2001, Monthly Notices of the Royal Astronomical Society, 320, L30

Merritt, D., Gualandris, A., & Mikkola, S. 2009, The Astrophysical Journal Letters, 693, L35

Middelberg, E., & Bach, U. 2008, Reports on Progress in Physics, 71, 066901

Mikkola, S., & Merritt, D. 2008, The Astronomical Journal, 135, 2398

Mikkola, S., & Palmer, P. 2000, Celestial Mechanics and Dynamical Astronomy, 77, 305

Miralda-Escudé, J., & Gould, A. 2000, The Astrophysical Journal, 545, 847

Miyoshi, M., Moran, J., Herrnstein, J., et al. 1995, Nature, 373, 127

Morris, M. 1993, The Astrophysical Journal, 408, 496

Morris, P. W., Eenens, P., Hanson, M. M., Conti, P. S., & Blum, R. 1996, The Astrophysical Journal, 470, 597

Moulton, F. R. 2012, An introduction to celestial mechanics (Courier Corporation)

Najarro, F., Hillier, D., Kudritzki, R., et al. 1994, Astronomy and Astrophysics, 285, 573

Najarro, F., Krabbe, A., Genzel, R., et al. 1997, Astronomy and Astrophysics, 325, 700

Natarajan, P., & Treister, E. 2009, Monthly Notices of the Royal Astronomical Society, 393, 838

O'Leary, R. M., Kocsis, B., & Loeb, A. 2009, Monthly Notices of the Royal Astronomical Society, 395

Pasham, D. R., Cenko, S. B., Zoghbi, A., et al. 2015, The Astrophysical Journal Letters, 811, L11

Pasham, D. R., Strohmayer, T. E., & Mushotzky, R. F. 2014, Nature, 513, 74

Peebles, P. 1972, The Astrophysical Journal, 178, 371

Perera, B. B. P., Stappers, B. W., Lyne, A. G., et al. 2017, Monthly Notices of the Royal Astronomical Society, 468, 2114

Perets, H. B., Gualandris, A., Kupi, G., Merritt, D., & Alexander, T. 2009, The Astrophysical Journal, 702, 884

Peters, P. C. 1964, Physical Review, 136, B1124

Press, W. H., Teukolsky, S. A., Vetterling, W. T., & Flannery, B. P. 1994, Cambridge: Cambridge University

Reid, M. J., & Brunthaler, A. 2004, The Astrophysical Journal, 616, 872

Reid, M. J., Readhead, A., Vermeulen, R. C., & Treuhaft, R. 1999, The Astrophysical Journal, 524, 816

Rein, H., & Liu, S.-F. 2012, Astronomy & Astrophysics, 537, A128

Rein, H., & Spiegel, D. S. 2014, Monthly Notices of the Royal Astronomical Society, 446, 1424

Rein, H., & Tamayo, D. 2015, Monthly Notices of the Royal Astronomical Society, 452, 376

Remillard, R. A., & McClintock, J. E. 2006, in Bulletin of the American Astronomical Society, Vol. 38, American Astronomical Society Meeting Abstracts, 903

Ruth, R. D. 1983, IEEE Trans. Nucl. Sci., 30, 2669

Saha, P., & Tremaine, S. 1992, The Astronomical Journal, 104, 1633

Salpeter, E. E. 1955, The Astrophysical Journal, 121, 161

Sandage, A. 1965, The Astropysical Journal, 141, 1560

Sani, E., Marconi, A., Hunt, L., & Risaliti, G. 2011, Monthly Notices of the Royal Astronomical Society, 413, 1479

Savorgnan, G., Graham, A. W., Marconi, A., et al. 2013, Monthly Notices of the Royal Astronomical Society, 434, 387

Schödel, R., Eckart, A., Iserlohe, C., Genzel, R., & Ott, T. 2005, The Astrophysical Journal Letters, 625, L111

Schödel, R., Ott, T., Genzel, R., et al. 2002, Nature, 419, 694

Schödel, R., Eckart, A., Alexander, T., et al. 2007, Astronomy & Astrophysics, 469, 125

Schubart, J. 1964, SAO special report, 149

—. 1968, The Astronomical Journal, 73

Shapiro, S. L. 1985, in Dynamics of Star Clusters, Vol. 113, 373–412

Shapiro, S. L., & Lightman, A. P. 1976, Nature, 262, 743

Spitzer Jr, L. 1969, The Astrophysical Journal, 158, L139

Tanaka, Y. a., Nandra, K., Fabian, A., et al. 1995, Nature, 375, 659

Thompson, A. R., Moran, J. M., & Swenson, G. W. 2001

Tremaine, S., Ostriker, J., & Spitzer Jr, L. 1975, The Astrophysical Journal, 196, 407

Tremaine, S., Richstone, D. O., Byun, Y.-I., et al. 1994, The Astronomical Journal, 107, 634

Van der Marel, R. P., & Anderson, J. 2010, The Astrophysical Journal, 710, 1063

Vaughan, S., & Uttley, P. 2005, Monthly Notices of the Royal Astronomical Society, 362, 235

Vika, M., Driver, S. P., Cameron, E., Kelvin, L., & Robotham, A. 2012, Monthly Notices of the Royal Astronomical Society, 419, 2264

Webster, B. L., & Murdin, P. 1972, Nature, 235, 37

Wisdom, J. 1982, The Astronomical Journal, 87, 577

—. 1983, Icarus, 56, 51

Wisdom, J., & Holman, M. 1991, The Astronomical Journal, 102, 1528

Wisdom, J., Holman, M., & Touma, J. 1996, Integration Algorithms and Classical Mechanics, 10, 217

Young, C. K., & Currie, M. J. 1994, Monthly Notices of the Royal Astronomical Society, 268, L11

Yu, Q., & Tremaine, S. 2003, The Astrophysical Journal, 599, 1129

Zwart, S. F. P., Baumgardt, H., McMillan, S. L. W., et al. 2006, The Astrophysical Journal, 641, 319

Zwart, S. F. P., & McMillan, S. L. 2002, The Astrophysical Journal, 576, 899

Zwart, S. F. P., McMillan, S. L., & Gerhard, O. 2003, The Astrophysical Journal, 593, 352

Zwart, S. P., Makino, J., McMillan, S. L., & Hut, P. 1998, arXiv preprint astro-ph/9812006